DETECTION OF SURFACE CORROSION BY ULTRASONIC BACKSCATTERING

A Thesis
Presented to
The George W. Woodruff School of Mechanical Engineering

By

Ghislain J. Retaureau

In Partial Fulfillment
Of the Requirements for the Degree
Master of Science in Mechanical Engineering

Georgia Institute of Technology

August, 2006

DETECTION OF SURFACE CORROSION BY ULTRASONIC BACKSCATTERING

Approved by:

Prof. Yves H. Berthelot, Advisor
School of Mechanical Engineering
Georgia Institute of Technology

Prof. Peter H. Rogers
School of Mechanical Engineering
Georgia Institute of Technology

Prof. Jennifer E. Michaels
School of Electrical and Computer Engineering
Georgia Institute of Technology

Date Approved: May 16, 2006

A mes parents,

«*Rien ne ressemble plus à ce qu'on nomme le hasard que ce qu'on nomme le nuage. Eh bien, les nuages sont exacts.* »

Hugo, Victor

ACKNOWLEDGEMENTS

I would like to thank my advisor Prof. Yves Berthelot for having taken me under his wings when I first came in Georgia Institute of Technology. Thanks to his support, I could have worked on this project with a lively interest. I would also like to thank Prof. Peter Rogers who believed in me when my days in Georgia Tech were in jeopardy.

I gratefully acknowledge Prof. Robert Mahan for his kindness and for helping me to find this thesis.

I would like to express my sincere appreciation to the people from Georgia Tech Research Institute: Michael Gray, John Doane, John Caspall and Ralph Herkert for their insight and contributions as this project has progressed.

TABLE OF CONTENTS

LIST OF TABLES

LIST OF FIGURES

LIST OF SYMBOLS AND ABBREVIATIONS

The entire document is written following the $+j$ convention.

A	:	Geometrical coefficient
α	:	Correlation length normalized by the wavelength
(α_A, β_A)	:	Couple of roughness and correlation length characterizing a surface A.
(α_B, β_B)	:	Couple of roughness and correlation length characterizing a surface B.
(α_C, β_C)	:	Couple of roughness and correlation length characterizing a surface C.
B	:	Geometrical coefficient
B	:	Global basis
BEM	:	Boundary Element Method
β	:	Roughness normalized by the wavelength or temporary variable used in the Ogilvy's demonstration.
CVI	:	Color Visible Imaging
C	:	Geometrical coefficient
c	:	Sound speed in the fluid
cos	:	Cosine function
χ	:	Characteristic function of the surface
χ_2	:	
D	:	Domain in presence of the insonified area only
d	:	Distance between the center of the emitter and the center of the insonified spot
d_{mn}	:	Distance between two realizations *m* and *n* in the RMS space or correlation space
$d\vec{r}_0$	:	Describes any element or sub-element of D.
$d\partial D$	:	Element of ∂D
$d\partial D_0$	:	Element of ∂D when the integration is carried by $\vec{r}_0$.
$d\partial\overline{D}$	:	Element of $\partial\overline{D}$
Δf	:	Sampling step in the frequency domain
$\Delta\vec{v}_1$	:	Tangent vector of a surface element along the x_1-axis

$\Delta\vec{v}_2$	:	Tangent vector of a surface element along the x_2-axis
Δx_1	:	Small segment (or sampling step) along the x_1-axis
Δx_2	:	Small segment (or sampling step) along the x_2-axis
$\Delta\partial D$	:	Small partition of ∂D
∂D	:	Insonified area
∂D^{∞}	:	Infinite rough plate
$\partial\overline{D}$	:	Mean plane of the insonified area
∂_{n0}	:	Normal derivative taken at a specific location pointed by $\vec{r}_0$, $\partial_{n0} = \vec{\nabla}_0 \cdot \ldots \vec{n}(\vec{r}_0)$.
$\frac{\partial^2}{\partial x^2}$	:	Partial derivative of order 2 with respect to x
$\frac{\partial^2}{\partial t^2}$	:	Partial derivative of order 2 with respect to time
E	:	Echo signal
$\sqrt{\overline{E^2}}$	:	RMS value of the Echo signal
EIS	:	Electrochemical Impedance Spectroscopy
e	:	Base of the natural logarithm that defines the exponential function.
exp	:	Exponential function
$\vec{e}_1$	:	Unit vector collinear to the x_1-axis
$\vec{e}_2$	:	Unit vector collinear to the x_2-axis
$\vec{e}_3$	:	Unit vector collinear to the x_3-axis
Ξ	:	Cumulated normalized variance
F	:	Angular factor
f	:	Frequency
f_s	:	Sampling frequency
$\hat{f}$	:	Complex amplitude of the force field of the source
GTRI	:	Georgia Tech Research Institute
$\hat{G}$	:	Complex amplitude of the Green's function
g	:	Non-dimensional variance of the surface profile
γ	:	Temporary variable used in the Ogilvy's demonstration.
γ_{ss}	:	Auto correlation function of the surface profile
$\vec{I}$	:	Acoustic Intensity
IRI	:	InfraRed Imaging or Thermography
$\mathrm{Im}\{\ \}$	:	Imaginary part operator
Inch," or in	:	Inch = 0.0254 m
$\langle I_d \rangle$	:	Average diffused intensity
$\langle I_d \rangle_{echo}$	:	Average diffused intensity measured from the wave scattered back to the emitter.
Idmax	:	Maximum intensity (usually in the specular direction)

i	:	Index, $i \in N$
j	:	Imaginary component
J	:	Jacobian
J_0	:	Bessel's function of order 0
kg	:	Kilogram
k	:	Wavenumber
$\vec{k}$	:	Wavevector
$\vec{k}_{inc}$	:	Incident wavevector
$\vec{k}_{sc}$	:	Wavevector of the scattered wave
k_{c0}	:	Characteristic wavenumber
$\vec{k}_0$	:	Dual vector of $\vec{r}_0$ in the Fourier space
k_{01}	:	Component of $\vec{k}_0$ along the k_1-axis in the wavenumber space
k_{02}	:	Component of $\vec{k}_0$ along the k_2-axis in the wavenumber space
k_{0i}	:	i-th component of $\vec{k}_0$
L_1	:	Length of the isonified rectangle
L_2	:	Width of the isonified rectangle
l	:	Focal length
lim	:	Limit operator
λ	:	Wavelength
λ_0	:	Lateral correlation length of the surface profile
λ_{01}	:	Correlation length along the x_1-axis
λ_{02}	:	Correlation length along the x_2-axis
MHz	:	Megahertz = $10^6 \mathrm{s}^{-1}$
max	:	Max function
m	:	Index, $m \in N$
N_t	:	Number of point in the time domain of a given sampled signal.
N_f	:	Number of point in the frequency domain of a given sampled signal.
n	:	Index, $n \in N$
n_1	:	First point of the echo signal
$\vec{n}$	:	Inward unit surface normal
$\vec{n}(\vec{r}_0)$	:	Surface normal at a specific location pointed by $\vec{r}_0$.
O	:	Origin
p	:	Acoustic pressure
$\hat{p}$	:	Complex amplitude of the acoustic pressure
p^{inc}	:	Incident pressure

$\hat{p}^{inc}$	:	Complex amplitude of the incident pressure
p^{sc}	:	scattered pressure
$\hat{p}^{sc}$	:	Complex amplitude of the scattered pressure
φ	:	Aperture angle of the emitter
$\hat{\mathrm{R}}$	:	Complex amplitude of the reflection coefficient
$\mathrm{Re}\{\ \}$	:	Real part operator
RMS	:	Root Mean Square
R	:	Ensemble of the real numbers
R_a	:	Average roughness
R_e	:	Transducer's radius, typically: $r_e = 0.25''$
R_p	:	Peak roughness
R_q	:	RMS roughness
R_t	:	Total roughness
R_v	:	Valley roughness
r	:	$\lvert\vec{r}\rvert$ or arbitrary distance
$\vec{r}$	:	Vector pointing on a domain point.
$\lvert\vec{r}-\vec{r}_c\rvert$	:	Distance between a domain point and the center of the insonified spot
$\lvert\vec{r}-\vec{r}_0\rvert$	:	Distance between a domain point and a surface point
$\vec{r}_c$	:	Points on the center of the insonified spot.
$\vec{r}_0$	:	Vector pointing on a surface point.
$\vec{r}_1$	:	Auxiliary vector analog to $\vec{r}_0$
Round	:	Function that rounds a number to the nearest integer.
ρ	:	Fluid density
SAW	:	Surface Acoustic Wave
SNR	:	Signal to Noise Ratio
s	:	Second
s	:	Surface profile
$\bar{s}$	:	Mean line
sin	:	Sine function
σ	:	Variance of the surface profile or RMS roughness
$\sum$	:	Sum operator
t	:	Time variable
θ	:	Polar angle in a cylindrical basis
θ_1	:	Angle of incidence
θ_2	:	Polar angle locating a domain point.
θ_3	:	Azimuth angle locating a domain point.
x_1	:	Coordinate of a domain point along the x_1-axis
x_2	:	Coordinate of a domain point along the x_2-axis

x_3	:	Coordinate of a domain point along the x_3-axis
x_{10}	:	Coordinate of a surface point along the x_1-axis
x_{20}	:	Coordinate of a surface point along the x_2-axis
x_{30}	:	Coordinate of a surface point along the x_3-axis
x_{11}	:	Coordinate of a surface point (pointed by $\vec{r}_1$) along the x_1-axis
x_{21}	:	Coordinate of a surface point (pointed by $\vec{r}_1$) along the x_2-axis
x_{31}	:	Coordinate of a surface point (pointed by $\vec{r}_1$) along the x_3-axis
Λ	:	Area between cumulated variances
Λ_1	:	Λ computed for the Head of the Echo only.
Λ_2	:	Λ computed for the Torso of the Echo only.
Λ_3	:	Λ computed for the Tail of the Echo only.
$\vec{\nabla}$	:	Gradient operator $\vec{\nabla} = \begin{pmatrix} \partial / \partial x_1 \\ \partial / \partial x_2 \\ \partial / \partial x_3 \end{pmatrix}$
∇^2	:	Laplacian operator $\nabla^2 = \vec{\nabla} \cdot \vec{\nabla}$
$\vec{\nabla}_0$	:	Gradient taken at a specific location pointed by $\vec{r}_0$
$\bar{}$	:	Mean component
$\langle\ \rangle$	:	Average operator
$\times$	:	Vectorial product
$\cdot$	:	Dot product
*	:	Conjugate operator
$\lvert\ \rvert$	:	Absolute value, magnitude or distance
$\int$	:	Integration operator, for example $\int_{\partial D} d\partial D$ is the integration over ∂D.
$\wedge$	:	Complex amplitude issued from the Fourier transform in time space
∞	:	Infinite

SUMMARY

Corrosion often occurs in the inner aluminum lining of the HB-53 helicopter external fuel tank, resulting in fuel leaks. This project centers on developing an in-situ ultrasonic inspection technique to detect corroded areas inside the fuel tank. Due to the complexity of the composite structure of the tank, the ultrasonic inspection is carried out from inside the tank using a monostatic backscattering technique. The backscattered field contains information related to the insonified surface properties (surface roughness scales). Numerical predictions are implemented with a simplified model of backscattered intensity (Ogilvy, 1991). Experimental results are obtained on artificially corroded plates, and on the actual fuel tank of the HB-53 helicopter. Signal processing techniques (Envelope Correlation and Inverse Technique) are used to detect corroded surfaces with data obtained with a focused 10 MHz pulsed transducer.

CHAPTER 1

INTRODUCTION

This project has been initiated in response of jet fuel leaks observed in HB-53 helicopter fuel tanks. Even if the interior of the tank is treated against corrosion, any coating or stainless metals is likely to corrode after years of contact with a liquid. That is why fuel tanks start leaking due to the combination of stress and corrosion. Until now, the main technique used at the NAVY depot to detect fuel leakage was to fill up the tank with water and look at the eventual leakages from the outside of the structure. At this stage it is already too late, most of the structure is extremely damaged and the fuel tank has to be replaced, a cost that exceeds 250,000 dollars. Early detection of corrosion is therefore desirable. The main strategy resides into detecting surface corrosion that occurs inside the tank indicating a recent breakdown in the coating system. Georgia Institute of Technology[1] proposed to build a system capable to enter in the tank and proceed to the surface scanning. This involves the development of optimized ultrasonic techniques for a specific use in the HB-53 fuel tank. After considering common ultrasonic methods used in surface evaluation, the detection of surface corrosion based on backscattered ultrasound appears to be the most appropriate. Scattering from rough

[1] GTRI team under G. O'Neil and M. Gray, and Mechanical Engineering under Y. Berthelot.

random surfaces has already been studied in great details [1][2][3]: biological tissue characterization (See for example the research done by Claudio Pecorari), surfaces damages detection such as cracks [4] and corrosion. When ultrasound in incident upon a rough surface, it is scattered in various directions. The scattered wave carries pertinent information about the surface. A particular attention is paid to the wave that is scattered back to the emitter.

The following sections introduce the general corrosion problem observed on aircraft structure. Each monitoring technique commonly used in aircraft corrosion detection is briefly presented and followed by various studies on surface evaluation.

1.1. Corrosion in HB-53 Fuel Tank

The fuel tank is an axisymmetric shell with layered wall construction as shown on Figure 1.1. The focus of the current research effort is to provide a capability for early detection of the thin (1/32”) aluminum interior liner. Corrosion found in the HB-53 fuel tank is initially the result of a chemical reaction between jet fuel and the anodized aluminum [5].

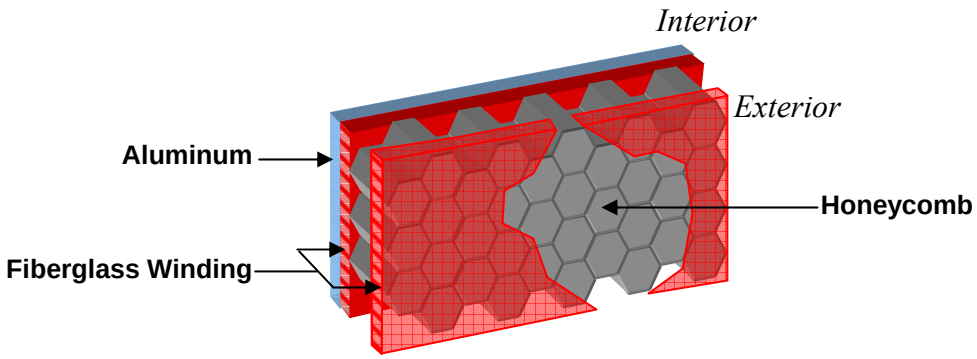

Figure 1.1 : Wall Structure

Even if anodizing aluminum makes its contact surface particularly stable regarding any oxidant, oxidation happens after years of usage. The aluminum interior liner gets corroded by dint of being in contact with jet fuel and impurities such as sand and sea minerals. Any scratch or machining mark can initiate local corrosion. In general corroded areas are observed at the bottom of the tank. Because of gravity, this part is also immersed longer and impurities mostly lie on this area.

Structural health is affected in three noticeable stages. First, the aluminum layer is subjected to a uniform corrosion. Local stains are visible and indicate the absence of an anodized layer. Once the anodized layer is removed, the jet fuel is directly in contact with aluminum. Then, the corrosion process intensifies and leads to advanced degradation by pit formation: this defines the second stage. Without treatments, pits turn into holes allowing jet fuel to propagate into sub layers such as fiber glass and honeycomb. The last stage is characterized by the most extreme case, when corrosion causes the fuel to leak out from the tank making it unusable. The following project proposes an early stage detection when corrosion occurs on the aluminum liner only. The next sections review corrosion types found in aircraft structures and ultrasonic monitoring techniques used to detect corrosion.

1.2. Types of Corrosion

Corrosion can be classified in twelve different forms according to three groups [6].

Table 1.1 : Corrosion Found in Aircrafts

Group 1: Identifiable by visual examination	Group 2: Requires additional devices	Group 3: Usually requires microscopy
Uniform Corrosion	Erosion	Environmental Cracking ▪ Stress Corrosion Cracking (SCC) ▪ Corrosion Fatigue ▪ Hydrogen Embrittlement
Pitting Corrosion	Cavitation	
Crevice Corrosion	Fretting Corrosion	
Galvanic Corrosion	Intergranular Corrosion	
Lamellar Corrosion	Exfoliation	
	Dealloying	

The types of corrosion mostly found in the fuel tank are shaded in Table 1.1. They are subsequently discussed in the next subsections.

1.2.1. Uniform Corrosion

By definition [7], uniform corrosion is characterized by a corrosive attack proceeding evenly over the entire surface area, or a large fraction of the total area. Surface corrosion can indicate a breakdown in the protective coating system. If surface corrosion is permitted to continue, the surface may become rough and surface corrosion can lead to more serious types of corrosion.

1.2.2. Pitting Corrosion

Pitting corrosion is a localized form of corrosion in which cavities are produced in the material. It often comes after uniform corrosion, representing areas that are privileged by the

corrosion process due to the non homogeneousness of the medium. Severe structural damage can be caused by the conjugation of pitting corrosion and stress.

1.2.3. Crevice Corrosion

Crevice corrosion is a localized form of corrosion usually associated with a stagnant oxidizing solution in crevices. A micro environment is created where aggressive ion species build up and degrade the surface.

All those types of corrosion contribute to the mass loss (thinning) of the shell. Moreover conjugated with important stress, those processes can lead to weaken areas or cracks in the structure. Corrosion monitoring techniques have been developed to identify corrosion on structures.

1.3. Corrosion Monitoring Techniques

Table 1.2 relates the most common techniques used to identify corrosion in aircrafts [8].

Table 1.2 : Corrosion Monitoring

Technique	Description
Visual and enhanced visual	Scheduled visual inspections are conducted by a human observer.
Eddy Current	Circulating magnetic fields are generated from a coil and propagate along the surface. Any type of inhomogeneity met on the surface modifies the magnetic field by a jump of magnetic permittivity resulting in the change of the coil impedance.
Ultrasonics	Corrosion is understood as a spatial perturbation that affects the mechanism of reflection and transmission of an acoustic wave at the interface.
Radiography	Is based on the transmission of X-Rays through the structure.
EIS (Electrochemical Impedance Spectroscopy)	Luigi Galvani showed that a corroded medium acts as an anode. The Frequency Response Function (FRF) is determined to estimate the anode current.
CVI (Color Visible Imaging)	The digitized image of the surface is evaluated with algorithms to find pits and cracks.
IRI (InfraRed Imaging or Thermography)	Corroded areas have a particular thermal conductivity. Therefore, the thermal gradient is visualized using an infrared camera when cooling or heating the structure.
Lamb Waves	Ultrasonic waves are generated in the structure; Propagation is affected by the medium (the structure).
Impedance Method	Waves are generated in the structure by piezoelectric transducers. There exists a coupling between transducers and the structure. Any homogeneity affects the electrical impedance of the piezoelectric.

Ultrasonics and visual techniques (shaded in Table 1.2) are used to evaluate the surface corrosion in the fuel tank. Pictures of the scanned area can be obtained from a camera which points toward the center of the insonified spot. Therefore it is possible to infer the presence of corrosion by superimposing video and ultrasound data. However, the ultrasonic method still has to be defined: a better clue is given in the next part concerning some studies dedicated in corrosion detection using ultrasound.

1.4. Corrosion Detection by Ultrasound: State of the Art

The degradation of the structure by corrosion results in a random increase of surface roughness. Hence, a rough surface is perceived by the acoustic wave as a random boundary on which reflection and transmission occur.

Among the considerable work done on surface evaluation using ultrasonics, the following paragraphs refer to a selection of some interesting investigations. The presentation of the methods starts away from the surface with studies on backscattering, then gets closer to the boundary with leaky wave approaches and ends in the structure itself with transmission.

A great contribution on the study of the scattered intensity has been brought by J. A. Ogilvy in her book entitled “Theory of Wave Scattering from Random Rough Surfaces” [9]. The surface roughness is treated as a disturbance in space; therefore the perturbation theory is applied on the acoustic problem using the Kirchhoff-Helmholtz integral to find out the scattered intensity in the domain as a function of frequency, roughness height and lateral correlation length of the surface profile. The surface is thus assumed to be Gaussian. Ogilvy’s model of scattering is restricted to surfaces with small slopes and small roughness scales where local planar reflection can be applied involving a far field approximation. It is also

preferable to avoid high incidence (grazing) angle where the model tends to fail. In addition, the Kirchhoff theory used in this approach is known to violate energy conservation principle. However, comparisons with experiments show that the model presented by J. A. Ogilvy is concise and very efficient in its domain of validity. The model is presented in more details in Chapter 3.

A relevant time–frequency study on the pressure backscattered by a rough surface is done by Serge Dos Santos, Pierre Maréchal, François Vander-Meulen and Marc Lethiecq. The authors investigate ultrasonic backscattering from a surface in translation [10]. An emitter and a receiver are both coupled and tilted such that only backscattered pressure is measured. Due to the reflection and the translation properties, the time signal is somehow related to the spatial surface profile. Its amplitude is likely to increase when the insonified area becomes corroded. Estimators such as variance, skewness and kurtosis applied on the time waveform depend on surface roughness. The kurtosis is found to be the best indicator for corrosion detection by its intelligibility. Concerning the frequency domain, roughness effect manifests itself by a broadening of the spectrum. However the frequency analysis suffers from a lack of accuracy in the localization of the corroded area due to its duality with time. A large time signal would give a better frequency resolution resulting in space incertitude. Note that the implementation of this system is cheap and simple for two reasons: the two transducers can be substituted to a single one using a pulse Echo measurement. In addition, if the demodulated spectrum is contained into [0; 20] kHz, a common audio card is sufficient to digitize the signals.

Another technique used to quantify the effect of surface roughness concerns surface acoustic waves (SAW). Several studies deal with leaky SAW in the domain of the acoustic microscopy [11][12][13][14]. If the angle of incidence is judiciously chosen the

superimposition of the incident and reflected wave excites a wave that propagates along the surface. In those conditions this wave is said to be leaky because a part of its energy is reradiated into the fluid domain. The leak rate depends also on the surface roughness. Claudio Pecorari and G Andrew D. Briggs have developed a pertinent theory and conducted experiments to characterize the dispersion of those waves when propagating on randomly rough surfaces [15]. Calculations and experiments are done on small roughness scales (the order of magnitude is 2-10µm). The authors used a second-order perturbation approach and found theoretically that the velocity of the surface wave drops as the surface roughness increases: a 0.7% drop is observed for an aluminum-water interface according to the range of study. They also warn against stiff materials such as alumina where the process becomes less sensitive.

A very interesting work conducted by Peter B. Nagy and Joe H. Rose [16] concerns the detection of subsurface scatterers in presence of a rough surface. The understanding of this technique can be useful to detect hidden corrosion. Even if this study is mainly focused on the transmission process, it describes reflection and transmission for both coherent and incoherent components. Particular care is given to waves in the fluid medium as they represent a small fraction of the incident energy and constitute the key element of subsurface scattered detection. The authors use the phase screen approximation to predict the effects of surface roughness assuming that the surface height variations mostly induce phase changes on the velocity fields. Reflected waves in the fluid as well as longitudinal and shear waves in the material are found according to this assumption. The results are confronted with the second order perturbation method [2] and it turns out that the phase screen approximation is reasonably accurate to quantify the surface roughness induced attenuation on reflected and transmitted waves except at longitudinal critical angle. Those losses are related to the square

of the product between RMS roughness and frequency. Elastic properties and incident angle intervenes in a second factor. Universal loss functions are obtained and validated by experiments for some typical ranges of incident angle. The authors pay also attention to the scattering noise generated by the medium itself due to the granularity. In this model, the scattering process is interpreted as a noise that degrades coherent measurements especially for the detection of subscatterers. Numerical predictions and measurements indicates that the changes brought by surface roughness become substantial at high frequencies or very rough surfaces.

Hidden corrosion can be also detected using two wedge transducers. W. Zhu, J.L. Rose, J.N. Barshinger and V.S.Agarwala from Pennsylvania University propose a contribution to the study of hidden corrosion detection [17]. The structure is comparable as a guide in which ultrasonic waves propagate. Wave modes are cut off when they pass through a corroded section. Transmission and reflection coefficient can lead to determine corrosion depth of the corrosion defect if calibrated on a simple experiment or a BEM simulation. Because corrosion changes the velocity group and phase velocity, time of flight between the two transducers is also a good indicator to detect surface damages.

1.5. Practical Constraints

The surface inspection system that needs to be designed to detect corrosion in HB-53 fuel tanks has to satisfy some practical constraints. The system of detection has to proceed quickly; the sponsor wants the inspection to be done within a few hours.

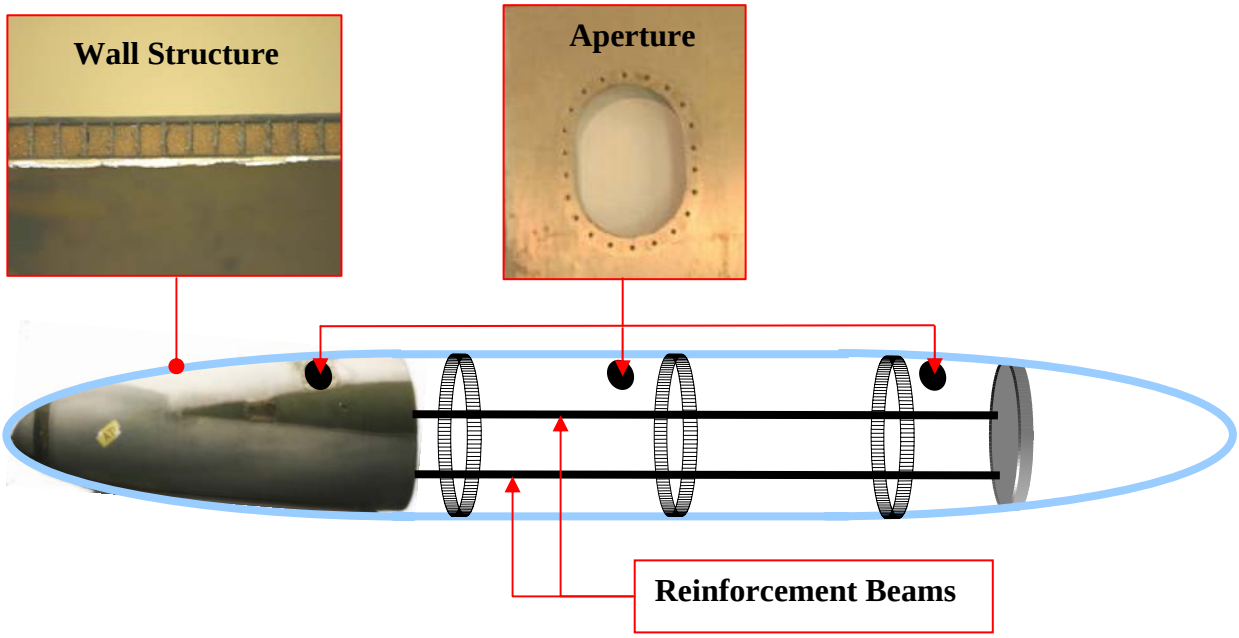

Figure 1.2 : Fuel Tank Stucture

Figure 1.2 shows the main parts of the tank structure. The complexity of the wall structure makes the measurements from the outside of the tank extremely difficult to characterize the integrity of the aluminum. Therefore, a method is developed to make measurements from the inside of the tank. The honeycombs present as a sub-layer add severe complications making any detection methods based on the wave propagation in the structure impossible. The entire system has to be small enough so that it can enter in the shell by the aperture used to fill up the tank. Because of the presence of reinforcement beams and ducts, it is preferred to opt for a non contact method so that the system can proceed to the surface scanning without being obstructed by those elements. The two reinforcement beams shown on the Figure 1.2 are chosen to support and guide the scanner. The scanning system has been designed by the GTRI team. This thesis concentrates on developing the ultrasonic system and data analysis needed to detect corrosion in the fuel tank.

Table 1.3 : Corrosion Detection Techniques by Ultrasonics

Technique	Disadvantages	Noticeable Advantages
Transmission and reflection in the structure	▪ Requires until two wedges transducers ▪ Contact method ▪ The wall structure of the tank complicates the propagation process.	None
Acoustic microscopy	▪ Measurements are extremely local ▪ Requires water couplant ▪ Subjected to be affected by the complexity of the wall structure.	None
SAW	▪ Weak, high leakage rate if no couplant ▪ Requires until two transducers	▪ Highly dependent on surface aspect. ▪ No contact with the surface
Scattered Pressure	▪ Requires two transducers	▪ Mostly dependent on surface aspect. ▪ No contact with the surface
Backscattered Pressure	▪ Data is collected at the incident angle only.	▪ Mostly dependent on surface aspect. ▪ No contact with the surface ▪ Compact

Table 1.3 summarizes various ultrasonic approaches for the detection of corrosion. After eliminating some of the techniques because of practical constrains for our geometry, the surface roughness evaluation by backscattering seems to be the most promising approach. The backscattered pressure is affected by surface roughness and it requires only one transducer. The technique requires of course a fluid medium, e.g. water, where ultrasonic waves can propagate from the transducer to the structure with minimum attenuation.

CHAPTER 2

SCATTERING FROM ROUGH SURFACES

The study of wave scattering from rough surfaces involves some basic concepts that are introduced in this chapter.

2.1. Description of the Problem and Formalism

The nomenclatures as well as the assumptions used to describe the configuration are presented in this section. The following notations are kept the same in the entire document.

2.1.1. Geometry

A defined global frame is composed by a direct basis $B:(\vec{e}_1,\vec{e}_2,\vec{e}_3)$ and an origin O that describes a three dimensional continuous space R^3. All locations (x_1,x_2,x_3) in this space are pointed from the origin O by a vector $\vec{r}=\begin{pmatrix}x_1\\x_2\\x_3\end{pmatrix}_B$ whose polar and azimuth angles are respectively denoted by θ_2 and θ_3. $\vec{r}$ can include a subscript depending on the entity (source,

surface point...) it points toward. The domain D is defined as the positive partition[2] of R^3 that is delimited by a random boundary ∂D^∞ (Figure 2.1).

- The origin is chosen such that it belongs to the mean plane $\partial \overline{D}^\infty$
- The orientation of $\vec{e}_3$ is chosen so that the x_3-axis is perpendicular to the mean plane

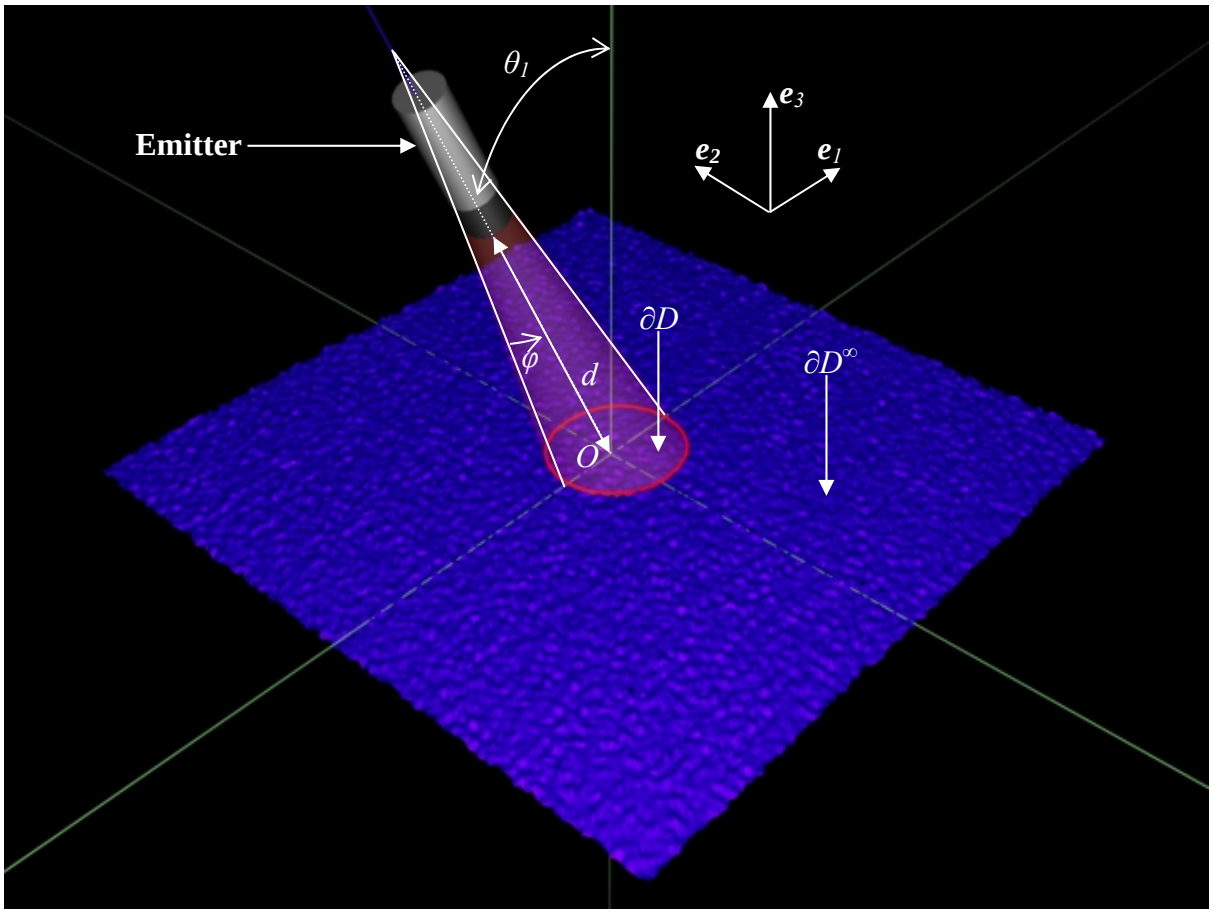

Figure 2.1 : Ultrasonic Scanning at Oblique Incidence

∂D^∞ is an infinite rough plate immerged into a fluid whose density is ρ and sound speed c. Only a limited area ∂D of this surface is insonified by an emitter. The mean plane of the

[2] If a space is partitioned, inward normal vectors of a boundary point inside a given partition which is said to be "positive" (see for example Hand Book of Graph Theory by Jonathan L Gross and Jay Yellen).

insonified area is denoted $\partial\overline{D}$. The emitter is a circular vibrating surface of radius R_e which center is distant of d from the center of the insonified spot (Origin). It is tilted of an angle θ_1 sufficiently small to avoid grazing waves.

2.1.2. Fluid

The fluid is water whose density is $\rho = 1000\,\mathrm{kg}\cdot\mathrm{m}^{-3}$ and whose sound speed c is equal to $1500\,\mathrm{m}\cdot\mathrm{s}^{-1}$. It is a non viscous fluid loaded on an impenetrable surface and affected by small pressure perturbations. Thus, those assumptions lead to the following:

- Shear waves are not treated in the model.
- Linear acoustics is applied
- Surface waves are not taken in account

Outside the source region, the propagation of acoustic waves in the fluid is governed by the wave equation:

$$\nabla^2 p(\vec{r},t) - \frac{1}{c^2}\frac{\partial^2 p(\vec{r},t)}{\partial t^2} = 0 \ . \qquad \textit{Eq 2.1}$$

2.2. Description of Rough Surfaces

2.2.1. Mean Line and Roughness Height

The roughness and the mean line are measured on a relevant portion ∂D of the surface. ∂D can be a segment or a finite surface. For a non inclined plate, the mean line $\bar{s}$ is defined by its height which is the average of the surface profile s:

$$\bar{s} = \frac{1}{\partial D} \int_{\partial D} s(x_1, x_2) d\partial D . \qquad \textit{Eq 2.2}$$

The average roughness R_a is the area between the profile and its mean line is also called the standard mean deviation:

$$R_a = \frac{1}{\partial D} \int_{\partial D} \left| s(x_1, x_2) - \bar{s} \right| d\partial D . \qquad \textit{Eq 2.3}$$

R_a is the most commonly used parameter in random surface measurement. The earliest devices made to evaluate random surface properties used a stylus and analog electronics to compute the absolute value (diode bridge) and integrate the electric signal while scanning (capacitance).

The RMS roughness σ also denoted R_q is the square root of the variance of the profile defined by:

$$\sigma^2 = \frac{1}{\partial D} \int_{\partial D} \left(s(x_1, x_2) - \bar{s} \right)^2 d\partial D . \qquad \textit{Eq 2.4}$$

This is the most relevant description for the roughness height of homogeneous random surfaces. R_q has completely supplanted R_a in metal machining specification because it is more relevant for the optical properties. Moreover, it is directly related to the variance of the roughness profile so that it is an entry for mathematical analysis. Other definitions of the surface roughness can be found in the literature such as peak roughness R_p, valley roughness

R_v and total roughness R_t. Because those parameters are not used in the study, they do not have to be defined. Nevertheless, those descriptions of the surface concern the height of the roughness profile; it does not give any information on the longitudinal axis.

2.2.2. Lateral Roughness Correlation Length

On Figure 2.2, the two following surface samples have the same RMS roughness and the same mean line height, but they seem to have different aspect. Profile 2 has higher slopes compared to Profile 1.

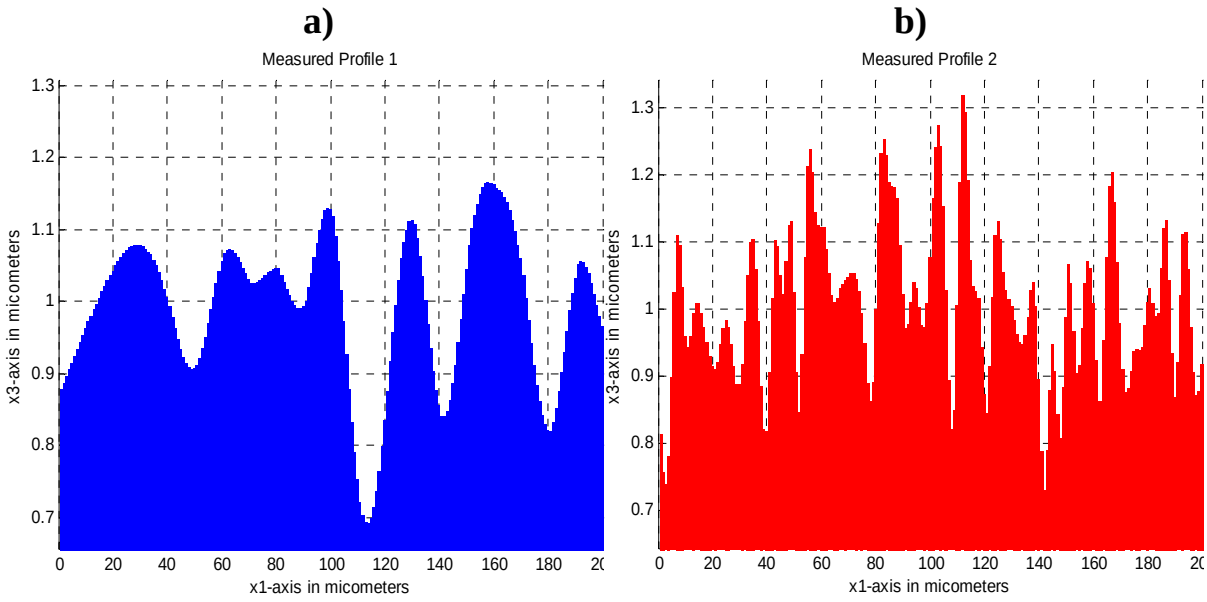

Figure 2.2 : Low and High Correlation Length Surface
a) Large Correlation Length, Profile 1**. b)** Small Correlation Length, Profile 2

The correlation length λ_0 is related to how the random patterns are stretched along the x_1-axis and x_2-axis. In general, correlation length is the distance from a point beyond which there is no further correlation of a physical property associated with that point. Values for a given property at distances beyond the correlation length can be considered purely random.

The definition of the correlation length involves the autocorrelation function of the roughness profile. It is the length for which the autocorrelation drops from its maximum (at zero) to its first local minimum. The autocorrelation functions of the profiles above have been plotted on Figure 2.3. Because the random patterns of Profile 1 are longer than for Profile 2, its correlation length is larger than the correlation length 2. For a two dimensional surface there are correlation lengths for each proper axis of the surface. λ_{01} and λ_{02} are the respective correlation lengths along the x_1-axis and the x_2-axis.

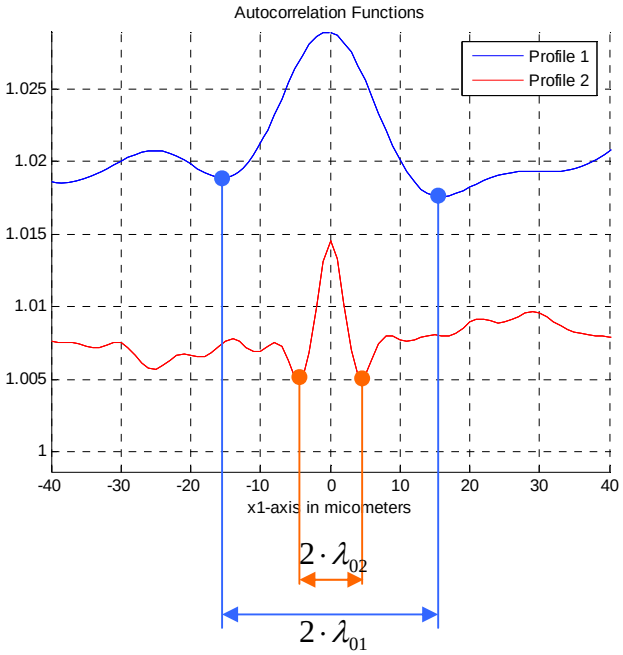

Figure 2.3 : Correlation Lengths

For a Gaussian surface, the correlation length is the distance over which the correlation function γ_{ss} drops by $1/e$:

$$\gamma_{ss}(r) = \exp(-r^2 / \lambda_0^2). \qquad \textit{Eq 2.5}$$

A particular care must be given to the type of correlation function algorithm used to compute the autocorrelation of the surface profile. Among the three types presented below, only the last two ones are acceptable for the determination of the correlation length.

- The linear cross correlation uses zero padding in order to double one of the two signals lengths. The second signal is shifted on the longest one proceeding to the integration at each shifting step (Figure 2.4). The output is a function that has the same number of points than the two input signals: linear cross correlation conserves the sample length. Nevertheless, the correlation function is **always** subjected to a window effect. A triangular envelope arises from the rectangular windows applied on the input signals (zero padding). Therefore the slopes of the correlation function are biased by this numerical artifact and may skew the determination of the correlation length.
- To avoid this window effect, the strict linear cross correlation requires the inputs signal to have different lengths. No zero padding is needed and the length of the output signal is the difference between the lengths of the two input signals (Figure 2.6). Strict linear cross correlation does not conserve the length but preserve the envelope.
- Another way to avoid the window effect is the circular cross correlation. The input signals are wrapped and rotated after each integration step (Figure 2.4). The length is conserved and the envelope is almost preserved. A discontinuity usually occurs when matching the beginning and the end of the signal. This discontinuity introduces an unexpected high frequency noise. Thus, it is advised against working with circular cross correlation algorithm when dealing with a frequency analysis.

a)

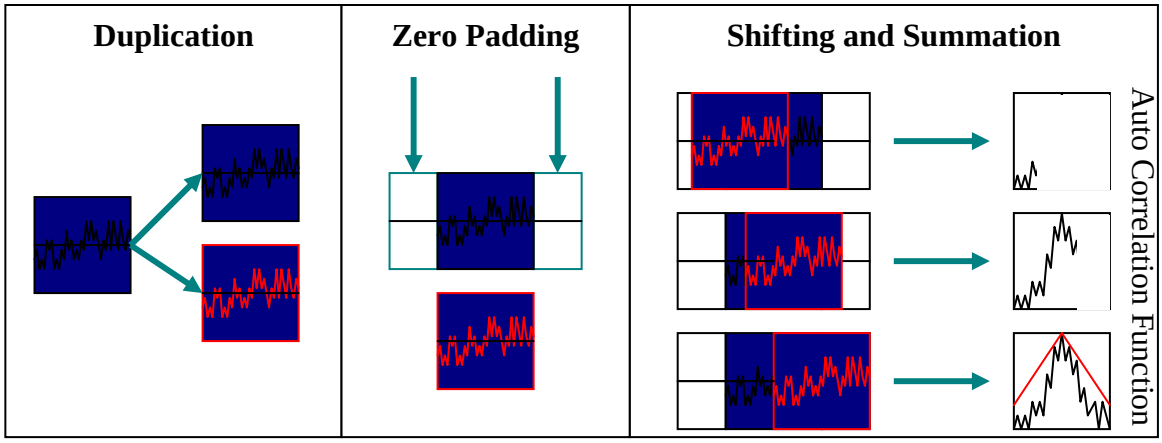

b)

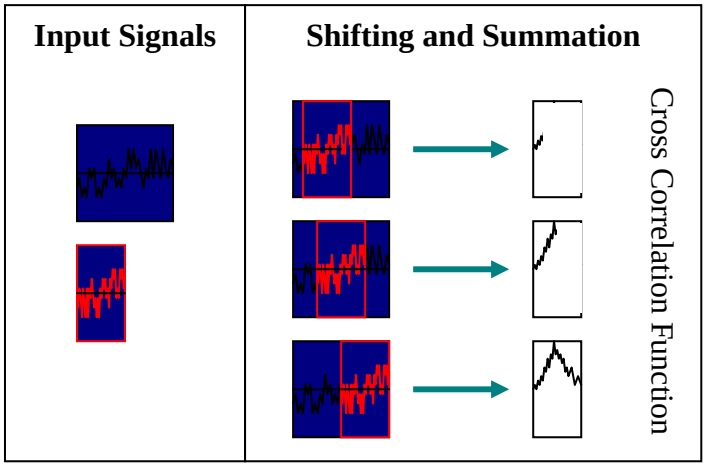

c)

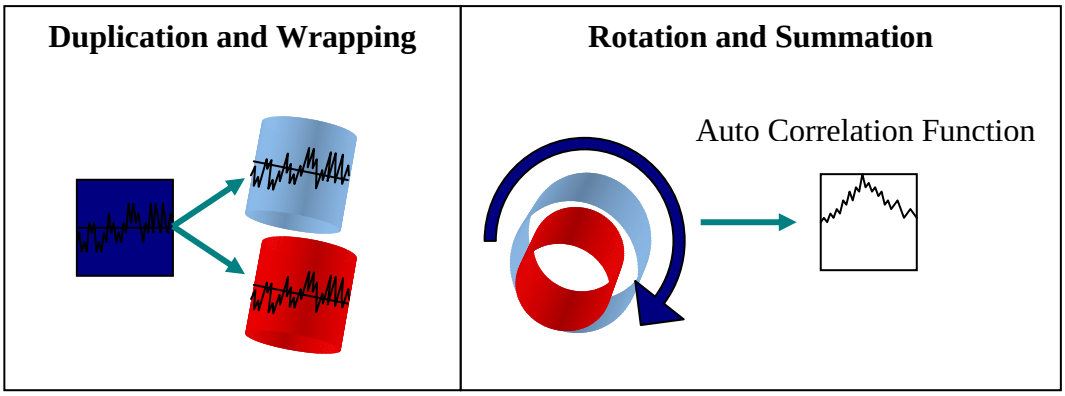

Figure 2.4 : Cross Correlations Computing Methods
a) Linear Autocorrelation. **b)** Strict Linear Cross Correlation. **c)** Circular Autocorrelation.

It is very important to specify that the estimators presented in this section are relevant if the surface is Gaussian or quasi-Gaussian. For certain non Gaussian surfaces this definition becomes obvious. The correlation functions are complicated and do not allow the correlation length to be determined easily according to this method. Then the global definition of the correlation length quoted at the beginning of this section is preferable. If the surface is random, its correlation function reaches a significant minimum at a shift which is the distance for two points of the profile to be assumed as uncorrelated.

2.2.3. Wavenumber Space

The spectrum representation is commonly used in physics of random phenomena. The random surface profile s is represented by its spectrum $\breve{s}$ into a dual space using a Fourier transform

$$\breve{s}(\vec{k}_0) = \int_{R^3} s(\vec{r}_0) \exp(-j\vec{k}_0 \cdot \vec{r}_0) d\vec{r}_0 \,. \qquad \textit{Eq 2.6}$$

$\vec{k}_0$ is a spatial frequency vector analog to a wavenumber, it involves two dimensions because the Fourier transform is carried on x_1 and x_2 axis. To become more familiar with spatial spectra, an example is taken on a Gaussian random surface with a $6.25 \cdot 10^{-4}$ m correlation length. The surface and its magnitude spectrum are plotted on Figure 2.5 and Figure 2.6.

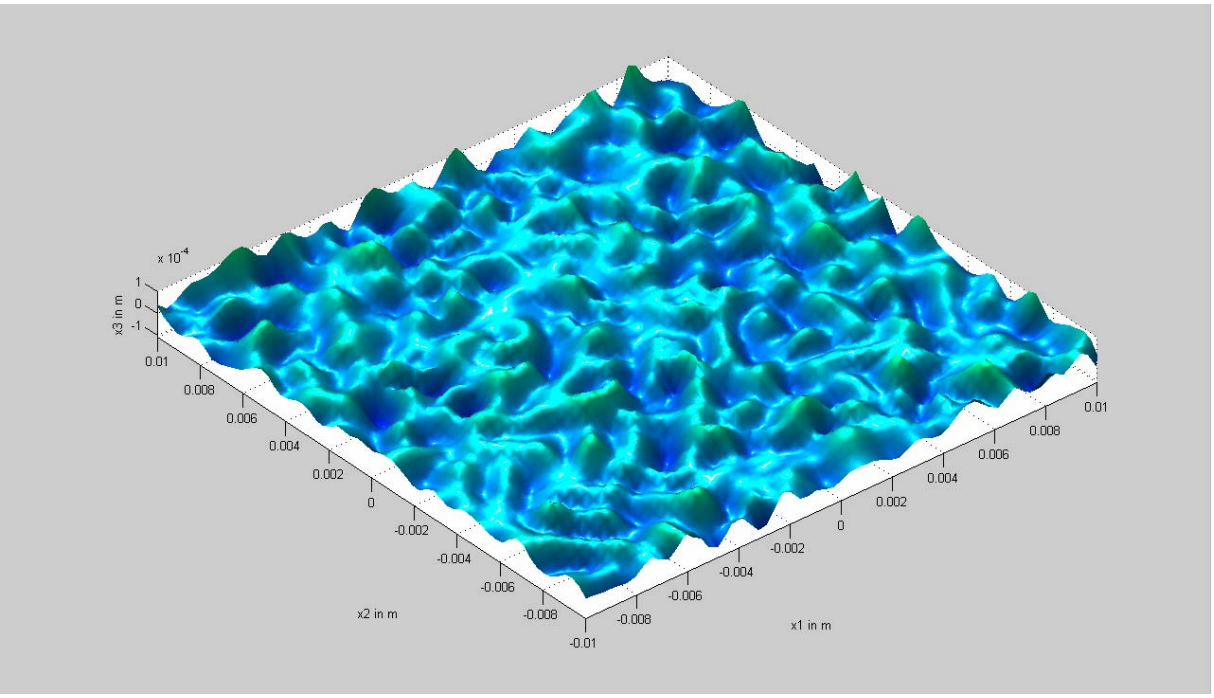

Figure 2.5 : Example of a Random Surface Generated by Using Matlab

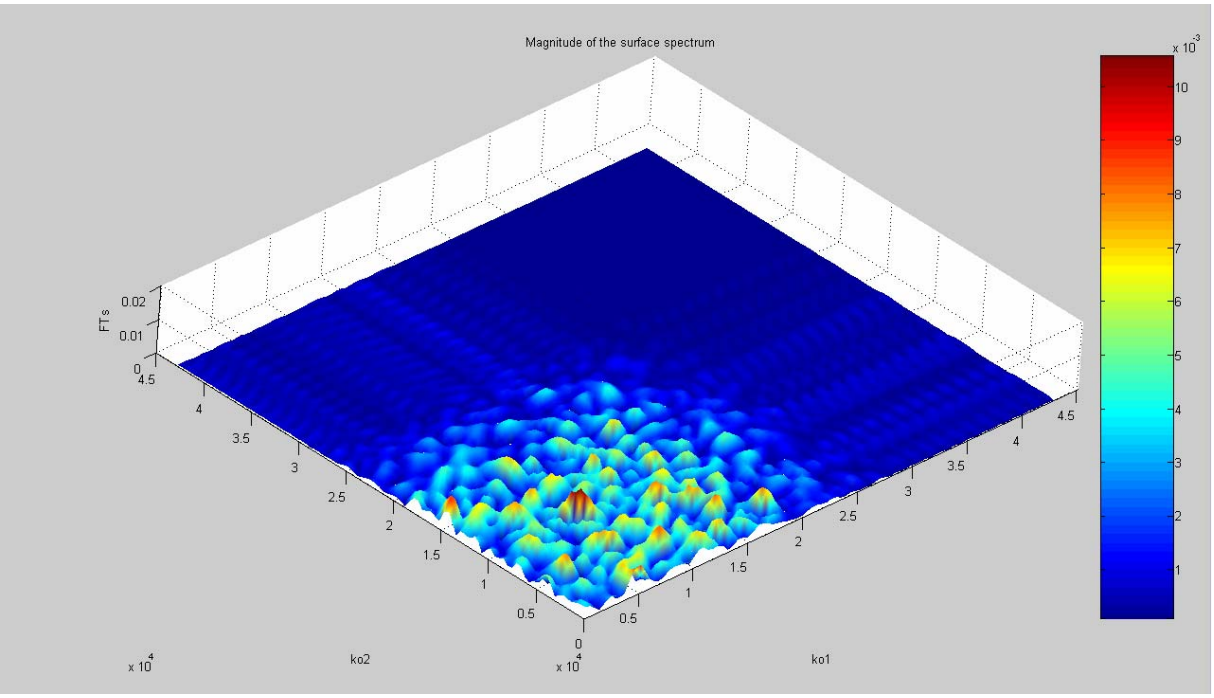

Figure 2.6 : Random Surface Spectrum

On the Figure 2.6 the initial amount of data has been quadrupled by zero padding. Because the surface is random, its spatial spectrum is bi-dimensional with a large bandwidth. It is also centered on its maximum reached at $k_0 \approx \frac{2\pi}{\lambda_0} = 10^4\,\mathrm{m}^{-1}$. The spectrum of a non Gaussian surface can have several local maxima. Hence many characteristic pattern lengths exist for a single surface and indicate that randomness occurs at different scales. Thus, in some critical cases the correlation length is not sufficient to characterize non Gaussian surfaces.

Generally, the spectrum of a random surface is expected to be centered on the characteristic wavenumber $k_{c0} = 2\pi / \lambda_0$. If the randomness is anisotropic, the single maximum is split into two maxima at $\frac{2\pi}{\lambda_{01}}$ and $\frac{2\pi}{\lambda_{02}}$ respectively. The periodic patterns that arise for $k_{0i} > 3 \cdot 10^4\,\mathrm{m}^{-1}$ are cardinal sines[3] issued from the windowing effect. Note that for a circular spot, those cardinal sinuses would be changed into Bessel's functions.

Also, the roughness is directly related to the amplitude range (dynamic) of the spectrum.

2.2.4. Discussion on Randomness

The notion of randomness has to be clarified. First, ideal randomness is a pure mathematical concept and is never found in nature. A process is said to be ideally random when no scale dominates. In consequence, the probability density function and the spectrum of an ideal random signal are constant. In reality, observed phenomena do not follow an ideal random process. Therefore any realistic process is said to be pseudo random, which means that successive events are not totally uncorrelated. Thus, the probability density function and the

[3] The cardinal sine function is defined as sinc(x) = sin(x)/x

spectrum are finite. In this study, the randomness arises from the corrosion process. This process involves the formation of aluminum oxide that leads to a specific corrosion pattern. The notion of characteristic or correlation length is directly related to the typical scale of the corrosion pattern. Figure 2.7 shows an aluminum surface corroded with muriatic (hydrochloridric) acid.

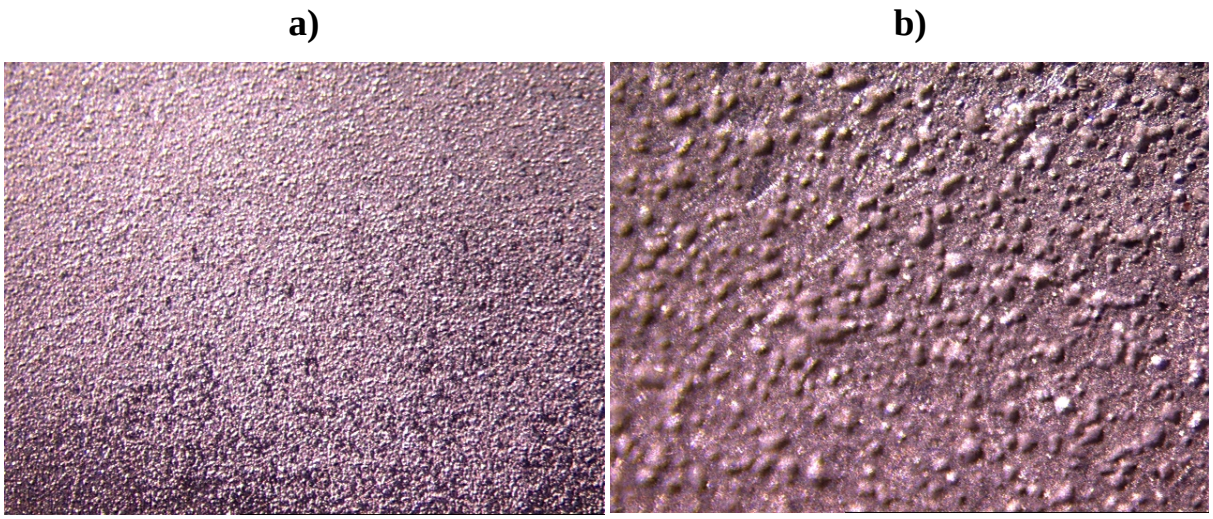

Figure 2.7 : Pictures of a Corroded Aluminum Surface
a) Corroded aluminum (Zoom = 2). **b)** Corroded aluminum (Zoom = 10).

Corrosion pattern vary with the type of oxidant and the status of corrosion, samples corroded with a chlorine solution[4] look different (Figure 2.8). This case is very unfavorable to assume a Gaussian surface analysis: pitting corrosion is not stationary and occurs on different scales.

[4] NaCl2(NCO3)2H20 + H20

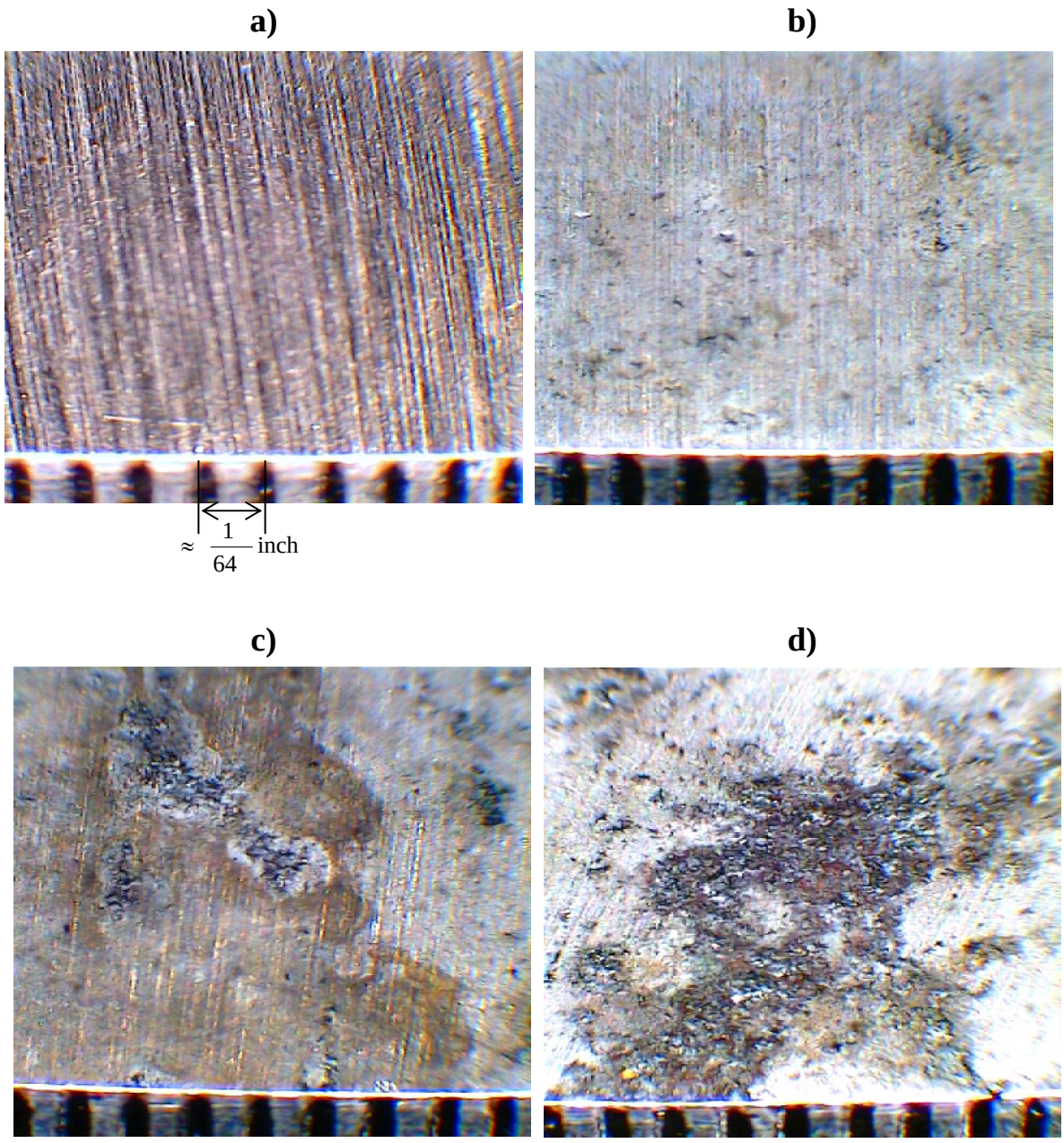

Figure 2.8 : Various Corrosion States of an Aluminum Sample Corroded with NaCl2(NCO3)2H20
a) Non-Corroded. **b)** Soft Corrosion. **c)** Medium Corrosion. **d)** High Corrosion

Figure 2.8 a): Not corroded. One can see the machine-made groves.

Figure 2.8 b): The sample is coated by a white, smooth layer of corrosion. There are also some little pits of corrosion (black stains).

Figure 2.8 c): The pits of corrosion are more important than the ones found in the previous sample.

Figure 2.8 d): The surface is composed of pronounced pits of corrosion.

CHAPTER 3

THEORETICAL APPROACH

This Chapter introduces the concept of wave scattering through an overview of the Kirchhoff theory. The theoretical model is used in further numerical simulations in order to illustrate the feasibility of some corrosion detection techniques.

3.1. The Helmholtz-Kirchhoff Integral

The Helmholtz-Kirchhoff integral of the acoustic problem is obtained by integrating the wave equation over the domain D. It is composed of a volume integral carried in the domain and a surface integral that allows boundary conditions to be applied. The form of this integral is given for outward surface normal in the frequency domain [18]:

$$\hat{p}(\vec{r}) = \int_D \hat{f}(\vec{r}_0)\hat{G}(\vec{r},\vec{r}_0)dD_0 - \int_{\partial D}\left(\hat{G}(\vec{r},\vec{r}_0)\partial_{n0}\hat{p}(\vec{r}_0) - \hat{p}(\vec{r}_0)\partial_{n0}\hat{G}(\vec{r},\vec{r}_0)\right)d\partial D_0 , \qquad Eq\ 3.1$$

where :

- $\vec{r}_0$ points toward the boundary ∂D of the domain D;
- $\vec{r}$ points toward a location in the domain D, also called domain point;
- $\hat{p}(\vec{r})$ is the complex amplitude of the pressure at that domain point;
- $\hat{f}(\vec{r}_0)$ is the force field that describes the source;
- Domain and boundary element are respectively denoted dD and $d\partial D$;
- $\hat{G}(\vec{r},\vec{r}_0)$ is the Green's function.

The problem is usually very difficult to solve because of coupling: the unknown is the pressure $\hat{p}$ that intervenes both in the integrand and as the single output variable. For some mathematical approaches, the second integral is a correction on the first integral which is non zero if the Green's function does not satisfy the exact boundary conditions.

The second integral can be split into the sum of the simple layer potential :

$-\int_{\partial D} \hat{p}(\vec{r}_0)\partial_{n0}\hat{G}(\vec{r},\vec{r}_0)d\partial D_0$ which is the jump of pressure passing thru the boundary.

and the double layer potential :

$\int_{\partial D} \hat{G}(\vec{r},\vec{r}_0)\partial_{n0}\hat{p}(\vec{r}_0)d\partial D_0$ which is the jump of velocity passing thru the boundary.

3.2. The Kirchhoff Theory

The Kirchhoff theory was originally used in optics for predicting diffraction of light by small holes. This theory has been extended in several fields including for scalar waves in acoustics where it is known to be a plane wave approximation (high frequency). In this study, Kirchhoff theory is applied for wave scattering in order to determine a fair model used to

describe the diffused intensity. The following demonstration can be found in « wave scattering from random rough surfaces » written by J.A. Ogilvy [9].

3.2.1. Emergence of the Scattered Pressure Field

Assume that the total pressure field is composed of the incident pressure and the scattered pressure:

$$p = p^{inc} + p^{sc}. \qquad \textit{Eq 3.2}$$

The Kirchhoff-Helmholtz integral is used to identify the scattered pressure field on condition that the Green's function is judiciously chosen. According to Equation 3.2 p^{sc} accounts for the specular reflection, the coherent and the incoherent scattered pressure. Therefore,

$$\hat{p}^{sc}(\vec{r}) = \int_{\partial D} \left(\hat{p}(\vec{r}_0)\vec{\nabla}_0 \hat{G}(\vec{r},\vec{r}_0) - \hat{G}(\vec{r},\vec{r}_0)\vec{\nabla}_0 \hat{p}(\vec{r}_0) \right) \cdot \vec{n}(\vec{r}_0) d\partial D_0 \qquad \textit{Eq 3.3}$$

with $\hat{G}(\vec{r},\vec{r}_0) = \dfrac{\exp\left(jk|\vec{r}-\vec{r}_0|\right)}{4\pi|\vec{r}-\vec{r}_0|}$. G is a free field Green's function such that:

-The first integral of the Kirchhoff-Helmholtz integral is the incident pressure field

-No sources of $\hat{p}^{inc}$ are on ∂D:

$$\int_{\partial D} \left(\hat{p}^{inc}(\vec{r}_0)\vec{\nabla}_0 \hat{G}(\vec{r},\vec{r}_0) - \hat{G}(\vec{r},\vec{r}_0)\vec{\nabla}_0 \hat{p}^{inc}(\vec{r}_0) \right) \cdot \vec{n}(\vec{r}_0) d\partial D_0 = 0. \qquad \textit{Eq 3.4}$$

In Equation 3.4 the pressure, the Green's function and their normal derivative have to be defined. The following section describes the assumptions made on those integrands to calculate the scattered pressure.

3.2.2. Far field Approximation

A far field approximation leads to keep the zeroth and the first order of the Taylor expansion of $k|\vec{r}-\vec{r}_0|$ such that the normal derivative of the Green's function may be rewritten as:

$$\vec{\nabla}_0 \hat{G}\cdot\vec{n} \approx j\frac{e^{jkr}}{4\pi r}\left(\vec{k}_{sc}\cdot\vec{n}\right)e^{-j\vec{k}_{sc}\cdot\vec{r}_0} \;\; if\; k|\vec{r}-\vec{r}_0| >> 1 \; and \; \vec{r} >> \vec{r}_0 \qquad Eq\ 3.5$$

where $\vec{k}_{sc} = k\vec{e}_r$ is the wavevector of the scattered wave.

3.2.3. Plane Wave Incidence

Assuming a plane wave incidence, the Kirchhoff approximation is used to find the pressure at the boundary and its derivative:

$$\hat{p} = \left[1+\hat{R}\right]\hat{p}^{inc} \qquad Eq\ 3.6$$

with $\hat{p}^{inc} = \exp(j\vec{k}_{inc}\cdot\vec{r})$.

Also the normal derivative is given by:

$$\vec{\nabla}\hat{p}\cdot\vec{n} = j\left[1-\hat{R}\right]\left(\vec{k}_{inc}\cdot\vec{n}\right)\hat{p}^{inc}. \qquad Eq\ 3.7$$

Finally Equation 3.3 can be rewritten as follows:

$$\hat{p}^{sc}(\vec{r}) = j\frac{e^{jkr}}{4\pi r}\int_{\partial D}\left(\hat{R}\left(\vec{k}_{inc}-\vec{k}_{sc}\right)-\left(\vec{k}_{sc}+\vec{k}_{inc}\right)\right)\cdot\vec{n}(\vec{r}_0)e^{j\left(\vec{k}_{inc}-\vec{k}_{sc}\right)\vec{r}_0}\,d\partial D_0 \,. \quad Eq\ 3.8$$

Note that the integration is carried on the real boundary which is random, because there is no description of the exact boundary, it is preferred to bring the integration on the mean plane.

3.2.4. Integration on the Mean Plane

Considering a surface element $\Delta\partial D$ pointed by $\vec{r}_0$: from the mean plane to the surface of the scatterer, this element has been tilted and stretched following Figure 3.1.

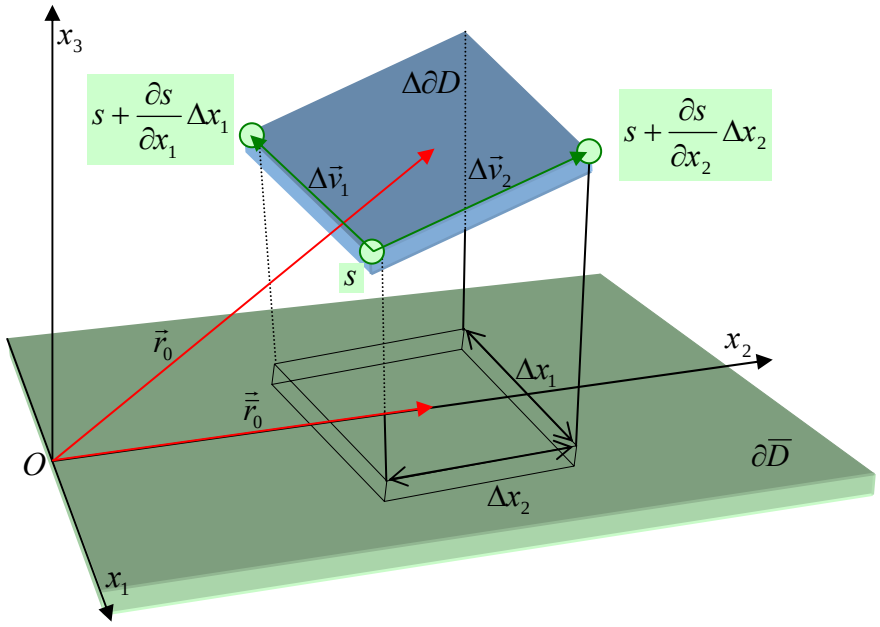

Figure 3.1 : Stretching of a Surface Element

The stretching coefficient is the ratio of the area before and after stretching. According to the sketch above, the element area $|\Delta\partial D|$ is defined by the cross product $|\Delta\partial D| = |\Delta\vec{v}_1 \times \Delta\vec{v}_2|$ with

$$\Delta\vec{v}_1 = \begin{pmatrix} x_1 + \Delta x_1 \\ x_2 \\ s + \frac{\partial s}{\partial x_1}\Delta x_1 \end{pmatrix} - \begin{pmatrix} x_1 \\ x_2 \\ s \end{pmatrix} = \Delta x_1 \begin{pmatrix} 1 \\ 0 \\ \partial s / \partial x_1 \end{pmatrix} \text{ and } \Delta\vec{v}_2 = \Delta x_2 \begin{pmatrix} 0 \\ 1 \\ \partial s / \partial x_2 \end{pmatrix}:$$

$$|\Delta\partial D| = \Delta x_1 \Delta x_2 \left| \begin{pmatrix} 1 \\ 0 \\ \partial s / \partial x_1 \end{pmatrix} \times \begin{pmatrix} 0 \\ 1 \\ \partial s / \partial x_2 \end{pmatrix} \right| = \Delta x_1 \Delta x_2 \sqrt{\left(\frac{\partial s}{\partial x_1}\right)^2 + \left(\frac{\partial s}{\partial x_2}\right)^2 + 1}. \qquad \textit{Eq 3.9}$$

Recall that:

$$\left| \begin{pmatrix} 1 \\ 0 \\ \partial s / \partial x_1 \end{pmatrix} \times \begin{pmatrix} 0 \\ 1 \\ \partial s / \partial x_2 \end{pmatrix} \right| = \begin{vmatrix} \frac{\partial}{\partial x_1} x_1 & \frac{\partial}{\partial x_2} x_1 \\ \frac{\partial}{\partial x_1} x_2 & \frac{\partial}{\partial x_2} x_2 \\ \frac{\partial}{\partial x_1} s & \frac{\partial}{\partial x_2} s \end{vmatrix} = |J(\vec{r})|. \qquad \textit{Eq 3.10}$$

J is the Jacobian of the vector $\vec{r}$ that points on the surface. The Jacobian is a useful operator that shows how an element has been stretched after a transformation. The surface profile can be taken as a result of a transformation that creates a random mesh from the original grid of points that defines the mean plane. In a quest of formalism, the limit $\Delta x \to 0$ is taken so that the surface element is noted:

$$d\partial D = d\partial\overline{D}\,|J(\vec{r}_0)|. \qquad \textit{Eq 3.11}$$

The inward unit vector is defined as:

$$\vec{n} = \frac{1}{\sqrt{\left(\frac{\partial s}{\partial x_1}\right)^2 + \left(\frac{\partial s}{\partial x_2}\right)^2 + 1}} \begin{pmatrix} -\partial s / \partial x_1 \\ -\partial s / \partial x_2 \\ 1 \end{pmatrix}. \qquad \textit{Eq 3.12}$$

Using Equation 3.11 and Equation 3.12, one finds that

$$\vec{n} d\partial D = \begin{pmatrix} -\partial s / \partial x_1 \\ -\partial s / \partial x_2 \\ 1 \end{pmatrix} d\partial \overline{D}\,. \qquad \textit{Eq 3.13}$$

The integration (Eq 3.8) is carried from the mean line. Some typical geometrical parameters can be identified when developing the dot product between the normal vector and the wavevectors. The scattered pressure is rewritten as :

$$\hat{p}^{sc}(\vec{r}) = j\frac{ke^{jkr}}{4\pi r}\iint_{\partial \overline{D}} \left(\alpha \frac{\partial s}{\partial x_{10}} + \beta \frac{\partial s}{\partial x_{20}} - \gamma\right) \exp\left(jk\left[Ax_{10} + Bx_{20} + Cs(x_{10}, x_{20})\right]\right) dx_{10} dx_{20}$$

Eq 3.14

where,

$A = \sin\theta_1 - \sin\theta_2 \cos\theta_3$;

$B = -\sin\theta_2 \sin\theta_3$;

$C = -\left(\cos\theta_1 + \cos\theta_2\right)$;

$$\beta = \sin\theta_2 \cos\theta_3 \left(1 + \hat{R}\right);$$

$$\gamma = \cos\theta_2 \left(1 + \hat{R}\right) - \cos\theta_1 \left(1 - \hat{R}\right).$$

A partial integration is performed in order to eliminate the terms that involve the surface gradients. $\partial\overline{D}$ is chosen to be a $2L_1 \times 2L_2$ rectangle.

$$\begin{aligned}\hat{p}^{sc}(\vec{r}) = -j\frac{ke^{jkr}}{4\pi r}\left(\frac{A\alpha}{C} + \frac{B\beta}{C} + \gamma\right)\int_{\partial\overline{D}} \exp\left(jk\left[Ax_{10} + Bx_{20} + Cs(x_{10}, x_{20})\right]\right)dx_{10}dx_{20} \\ - j\frac{ke^{jkr}}{4\pi r}\left(j\frac{\alpha}{kC}\int\left(\exp(jkAL_1) - \exp(-jkAL_1)\right)\exp\left(jk\left[Bx_{20} + Cs(x_{10}, x_{20})\right]\right)dx_{20}\right. \\ \left. + j\frac{\beta}{kC}\int\left(\exp(jkBL_2) - \exp(-jkBL_2)\right)\exp\left(jk\left[Ax_{10} + Cs(x_{10}, x_{20})\right]\right)dx_{10}\right)\end{aligned}$$

Eq 3.15

Note that the second term of the partial integration is related to the edges effects. It is assumed that the surface profile falls to zero at the edges such that $s(\pm L_1, \pm L_2) = 0$. The edges effects are therefore non stochastic and vanish out when calculating the average diffuse intensity in Equation 3.16:

$$\langle I_d \rangle = \left\langle \hat{p}^{sc}\left(\hat{p}^{sc}\right)^* \right\rangle - \left\langle \hat{p}^{sc} \right\rangle \left\langle \left(\hat{p}^{sc}\right)^* \right\rangle. \qquad \textit{Eq 3.16}$$

Note that this definition of intensity is valid when the far field condition is satisfied, some studies include a factor $\frac{1}{2\rho c}$: $\vec{I} = \frac{\hat{p}\hat{\vec{v}}^*}{2} = \frac{\hat{p}\hat{p}^*}{2\rho c}$. The average diffuse intensity is therefore:

$$\langle I_d \rangle = \frac{k^2}{(4\pi r)^2} 4F^2 \iint_{\partial\vec{D}^2} \left(\exp\left(jk\left[A(x_{10}-x_{11})+B(x_{20}-x_{21})\right]\right)\right.$$
$$\left.\left(\left\langle \exp\left(jkC\left[s(\vec{r}_0)-s(\vec{r}_1)\right]\right)\right\rangle - \left\langle \exp\left(jkCs(\vec{r}_0)\right)\right\rangle\left\langle \exp\left(jkCs(\vec{r}_1)\right)\right\rangle\right)\right) dx_{10}dx_{20}dx_{11}dx_{21}$$

Eq 3.17

Where $F = \frac{1}{2}\left(\frac{A\alpha}{C}+\frac{B\beta}{C}+c\right)$.

For an isotropic surface, the statistical properties are invariant by rotation such that the integration can be circular: $x_{10}-x_{11} = r\cos\theta$ and $x_{20}-x_{21} = r\sin\theta$:

$$\langle I_d \rangle = \frac{k^2}{(4\pi r)^2} 4F^2 \int_{-L_1}^{L_1}\int_{-L_2}^{L_2}\int_{0}^{2\pi}\int_{0}^{\max\left(\sqrt{x_{11}^2+x_{21}^2}\right)} \left(\exp\left(jk\left[Ar\cos\theta + Br\sin\theta\right]\right)\right.$$
$$\left.\left(\chi_2(kC,-kC,r) - \chi(kC)\chi^*(kC)\right)\right) dx_{11}dx_{21}rdrd\theta$$

Eq 3.18

where χ, χ_2 are respectively the one and two dimensional characteristic function. Those functions are provided by the Fourier transform of the probability density function of the surface profile. The third argument of χ_2 is the distance between two points of the surface upon which the probability density is evaluated. If the distance is small, those two points may appear as highly correlated. If the distance is greater than the correlation length, those two points are assumed to be non correlated such that the property of independence applies:

$$\chi_2(kC,-kC) \to \chi(kC)\chi^*(kC) \quad . \qquad \textit{Eq 3.19}$$

In order to have a consistent sample, the size of the insonified spot is much greater than the correlation length such that the integrands in Equation 3.18 tend to vanish at the limit of the integration. This is not an issue if the integral on *r* is carried from 0 to the infinity.

Typically for a Gaussian surface,

$$\chi_2(kC,-kC,r) = \exp\left(-\left[k^2C^2\sigma^2\left(1-\exp(-r^2/\lambda_0^2)\right)\right]\right) = e^{-g}\sum_{n=0}^{\infty}\frac{g^n}{n!}\exp(-nr^2/\lambda_0^2) \quad \textit{Eq 3.20}$$

with $g = k^2C^2\sigma^2$.

Therefore Equation 3.18 is may be rewritten as:

$$\langle I_d \rangle = \frac{k^2F^2e^{-g}}{2\pi r^2}\partial\overline{D}\sum_{n=1}^{\infty}\frac{g^n}{n!}\int_0^{\infty}J_0\left(kr\sqrt{A^2+B^2}\right)\exp\left(-nr^2/\lambda_0^2\right)rdr\,. \quad \textit{Eq 3.21}$$

Finally using an integration identity on the Bessel function J_0 it yields :

$$\langle I_d \rangle = \frac{k^2F^2\lambda_0^2e^{-g}}{4\pi r^2}\partial\overline{D}\sum_{n=1}^{\infty}\frac{g^n}{n!n}\exp\left(-\frac{k^2\left(A^2+B^2\right)\lambda_0^2}{4n}\right). \quad \textit{Eq 3.22}$$

k is the wavenumber of the incident ultrasonic beam;

F, A and B are purely geometrical factors;

λ_0 is the correlation length of the surface at the insonified spot.

g is the non-dimensional variance of the surface profile in terms of the incident wavemength;

$1/r^2$ is characteristic of the far field assumption for the scattered intensity

Equation 3.22 is straightforward to calculate the average intensity numerically.

CHAPTER 4

ULTRASONIC TECHNIQUE FOR THE DETECTION OF LINER CORROSION IN A HB-53 FUEL TANK

The model of wave scattering described in the previous chapter can be used to model the scattering process involved in the tank surface. Numerical results of this method are an important tool in the design of the specific system.

4.1. First Experimental Approach

4.1.1. Ultrasonic Device

The ultrasonic system is composed of 4 elements that are the signal generator, the transducer, the signal conditioner and the oscilloscope (Figure 4.2). As far as the ultrasonic

transducer is concerned (Figure 4.1), the frequency and the focus type are chosen depending on the roughness scale. According to the numerical result and the theoretical approach, large corrosion patterns are observed with a low frequency transducer in order to avoid too many details, whereas a smaller scale is measured by choosing a higher frequency. The picture below shows the set of five ultrasonic transducers used in the experiments.

Type	Typical Frequency	Focus
V306	2.5MHz	none
V306	2.5MHz	0.5 in
V309	5MHz	none
V309	5MHz	0.5 in
V311	10MHz	0.5 in

Diameter = 0.5 in
Except for the V306 unfocused

Figure 4.1 : Set of Panametrics Ultrasonic Transducers

The signal sent to the transducer is generated from a pulser that is composed of a signal generator and an amplifier. Even if the pulse delivered by the signal generator is short in time, the pulse wave that is sent in the fluid has a larger duration due to the internal structure if the transducer itself. The received signal can be amplified by an amplifier up to 40dB.

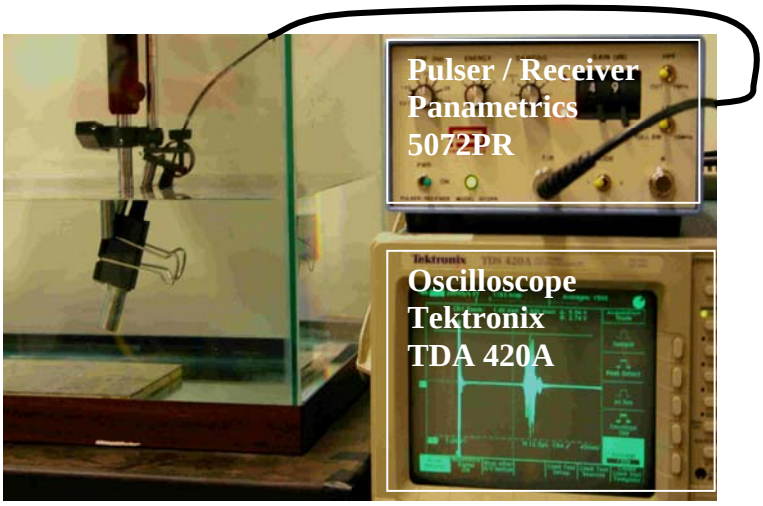

Figure 4.2 : Experimental Arrangement to Measure Ultrasonic Backscattering from Rough Surfaces

The oscilloscope is used to sample and store the data. The typical sampling frequency used for the Echo is 200MHz with a 8 bit resolution.

4.1.2. Sample Preparation

The purpose of this experiment is to become familiar with the use of each ultrasonic transducer in presence of a corroded aluminum plate. A of aluminum plate (6”x 12”) has been separated into four regions (6”x3”). The last three regions have been immersed in a solution with different chlorine concentration in order to get various depths of corrosion (Figure 4.3). The more the surface is corroded, the higher the roughness. The solution used to corrode those sample is composed of NaCl2(NCO3)2H20 diluted in water.

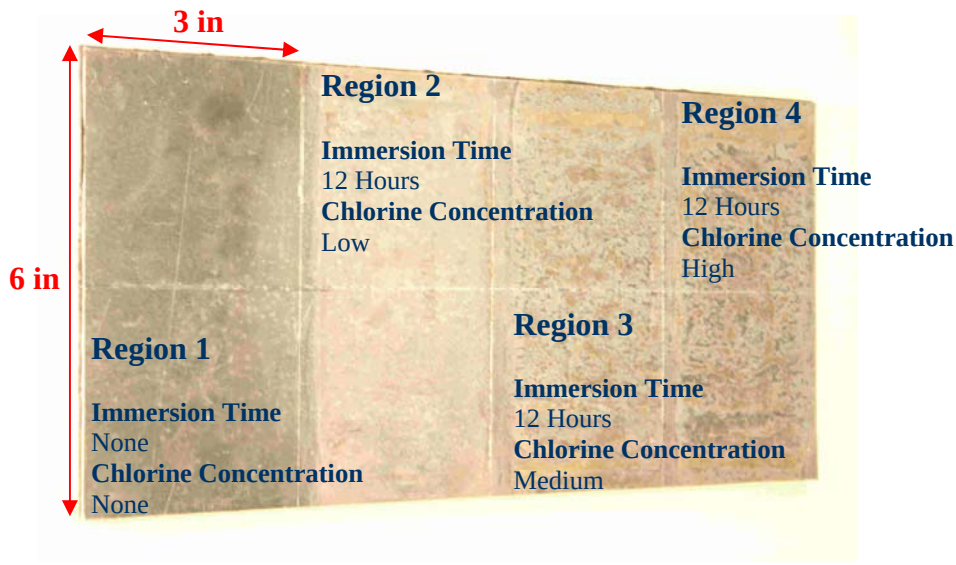

Figure 4.3 : Corroded Aluminum Sample

The sample obtained from this corrosion process is composed of four different areas within different surface roughness heights and correlation lengths (Table 4.1).

Table 4.1 : Sample Description

Region Number	Description of the surface
1	No corrosion, some soft stripes
2	Soft corrosion, uniform
3	Medium corrosion, non uniform with different patterns
4	High corrosion, non uniform with pronounced pits and different patterns

The areas are separated by a ~ 0.1'' groove which was initially used to separate the different solutions during the corrosion process.

Concerning the numerical prediction of the backscattered pressure of such a sample, it is not proper to use a probabilistic model if the corrosion is not uniform: this concerns Regions 3

and 4. When scanning those samples, the variations of the scattered pressure are important so that the expectation value itself is not relevant.

4.1.3. Measurements

An experimental study was conducted using a single 5 MHz transducer set in pulse-Echo mode. The angle between the transducer's acoustic beam axis and the plate surface normal is adjusted such that the field scattered back to the transducer is indicative of diffuse scattering due to the distribution of small scale surface features. According to the Rayleigh criterion[5], the higher the incident angle, the higher the backscattered energy. In addition, the transducer must be close enough to the surface. If the transducer is too close, some interactions between the structure of the transducer and the surface are observed when the transducer is set to an incidence higher than 60°. Figure 4.4 shows an Echo signal measured on a smooth plate: the spikes are related to the distance between the edges of the transducer and the surface and the radius of the emitter.

[5] The Rayleigh parameter given as $k\sigma\cos\theta_1$ described the apparent surface roughness experienced by the incident wave.

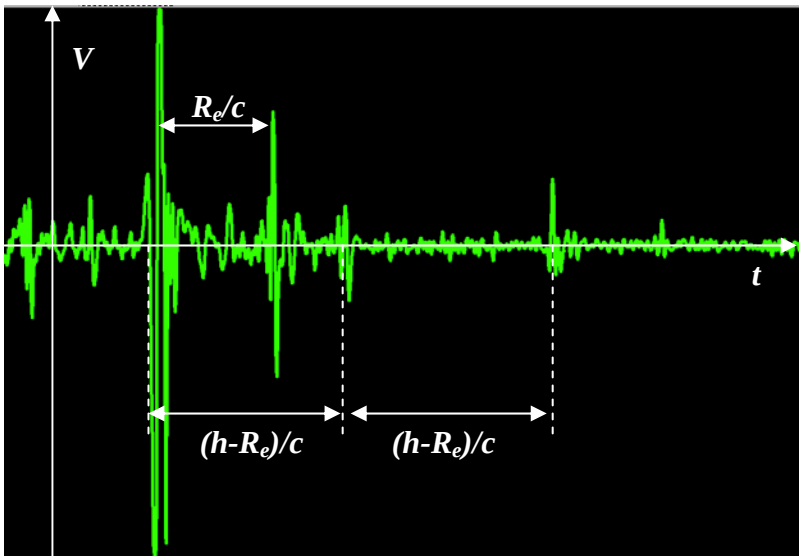

Figure 4.4 : Multiple Reflections between the Transducer and the Surface

The incident angle must large enough to avoid these spikes but not too close to the Rayleigh angle which is around 40°. This angle is also avoided as it is known that energy is trapped around the surface and transmitted in the aluminum layer such that the system more sensitive to subscatterers and the structure of the tank shell and very little energy is backscattered at this angle.

The distance between the center of the transducer and the surface has to be sufficiently small for the transducer to get significant backscattering. But if the distance is too small, the transducer is also likely to be on the way of the specular beam. Therefore a range of distance from the transducer to the surface is defined from 1 to 3 inches and the tilt angle is chosen at 25° for this range.

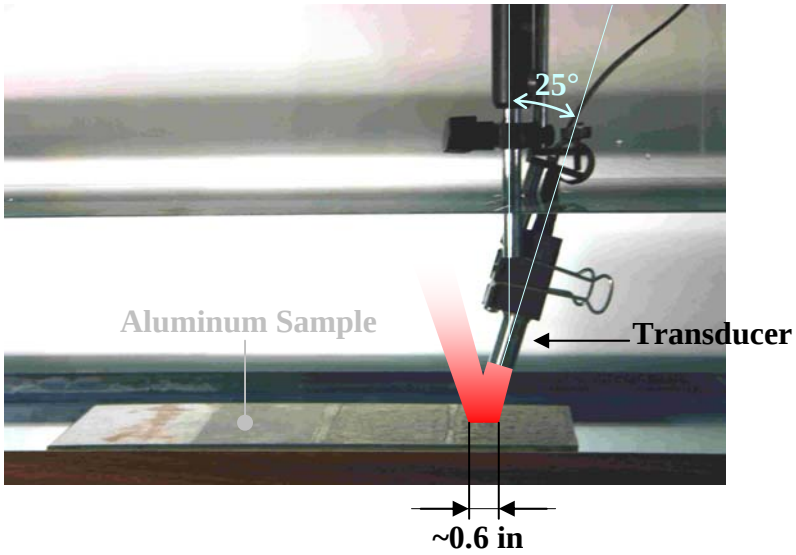

Figure 4.5 : Surface Examination Using a V309

A V309 unfocused transducer [19] translates along the x_1-axis at three inches from the surface, and data is acquired every 0.5 inch, which gives a total of 22 measurements (Figure 4.5). The purpose of this experiment is to find out the different type of corrosions with a Pulse-Echo analysis, and then to establish the best estimator that can differentiate corroded and non corroded surfaces.

4.1.4. Extraction of the Echo Signal

The entire time signal output by the pulser/receiver is displayed on Figure 4.6 for a typical surface measurement. The signal received by the transducer is amplified by 39 dB and the overall signal is averaged 100 times. The main bang pulse generated by the pulser is seen on the very left edge of the screen. This signal is mostly saturated. Buried in this saturated signal is the actual output of the transducer as well: this leading pulse is not exploitable and it is therefore preferable to work on the Echo signal $E(k)$ only.

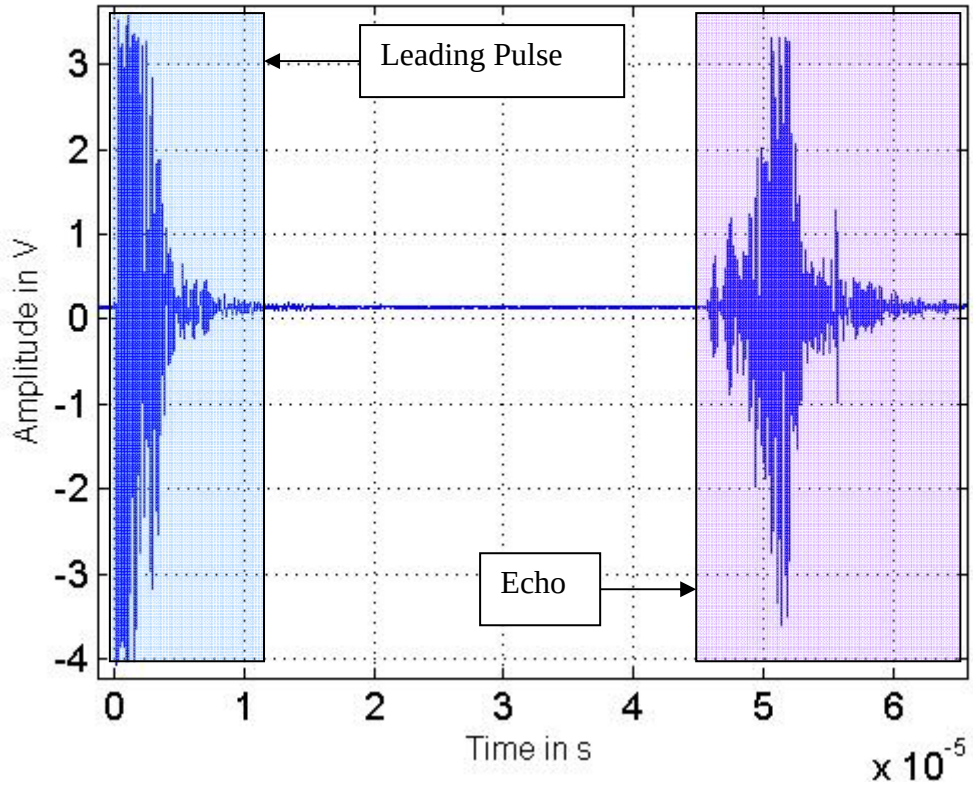

Figure 4.6 : Signal Output by the Pulser-Receiver

The time origin is taken at the very beginning of the bang pulse. The synchronization signal output from the 5072 PR drives the oscilloscope, therefore time index is set to zero at the beginning of every pulse (Figure 4.7).

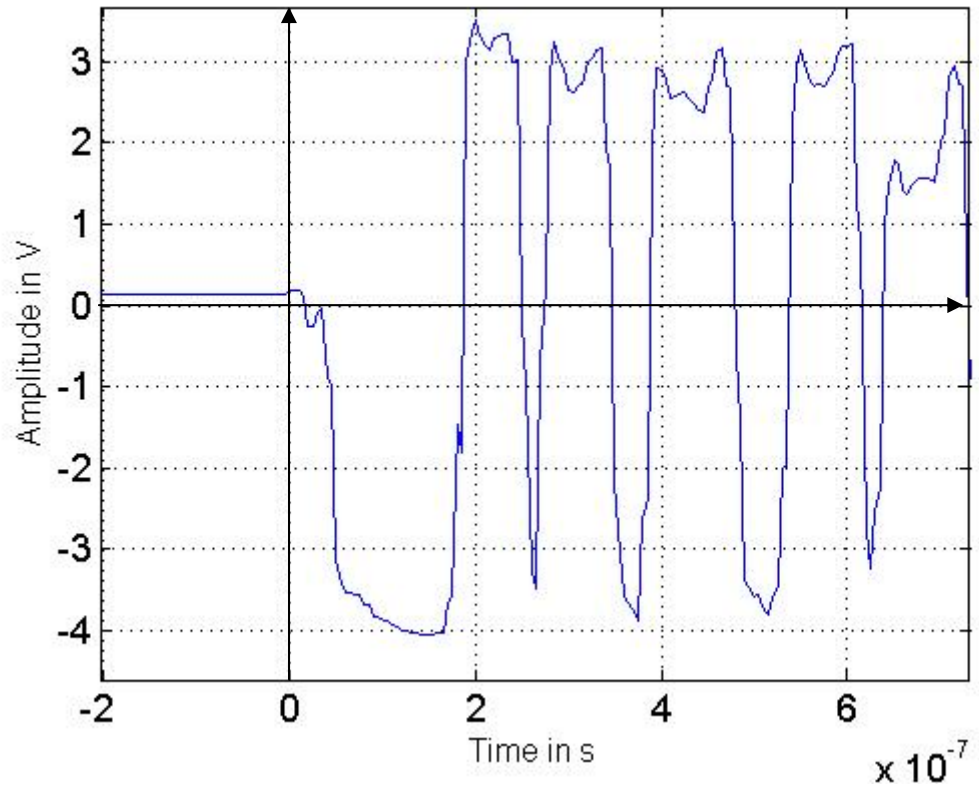

Figure 4.7 : Time Origin

The Echo signal is determined by calculating the time to travel for a round trip from the transducer to the surface. Proceeding by ray construction, The Figure 4.8 describes the geometrical problem which is solved to estimate the first point $n1$ of the Echo signal.

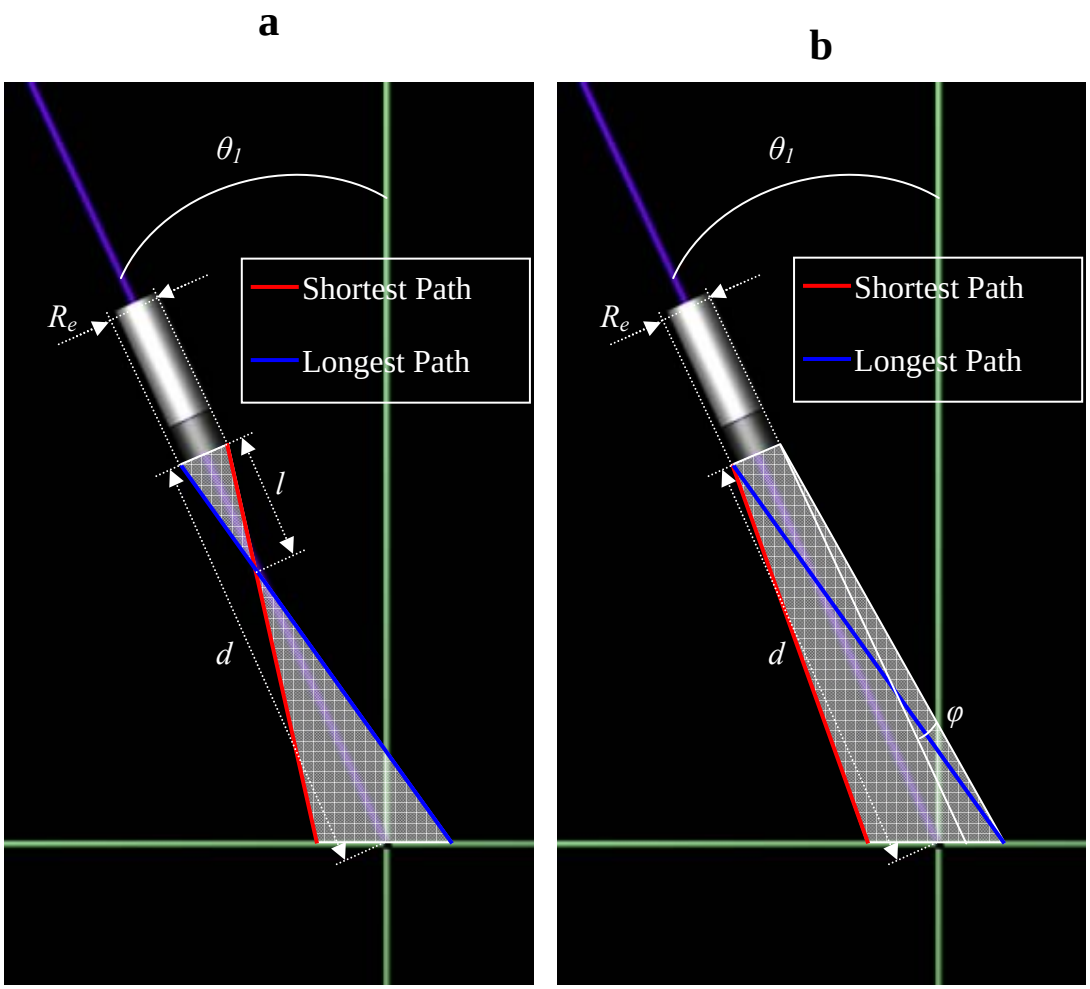

Figure 4.8 : Ray Construction Used to Estimate the Echo Signal
a) Focused Transducer. **b)** Unfocused Transducer.

For an unfocused transducer, the aperture angle φ is taken as 1°:

$$n1 = round\left\{\frac{2f_s}{c}\sqrt{d^2 + \left(R_e + d\tan\varphi\right)^2}\right\}. \qquad Eq\ 4.1$$

For a focused transducer whose focal length is l:

$$n1 = round\left\{\frac{2f_s}{c}\left(\sqrt{l^2 + R_e^2} + \frac{(d-l)\cos\theta_1}{\cos(\theta_1 - \arctan(R_e/l))}\right)\right\}. \qquad Eq\ 4.2$$

A rectangle window of length N_t is applied on the signal in order to extract to Echo waveform. According to the scanning configuration, the length of the Echo signal varies from 100 points to 3000 points.

In the frequency domain, the resolution of the Echo spectrum is mainly tributary of the size of the insonified spot. Equation 4.3 gives the number of points N_f that can be used for a frequency analysis:

$$N_f = \frac{\Delta f}{fs} N_t, \qquad Eq\ 4.3$$

where Δf is the frequency bandwidth of the transducer. The frequency resolution is typically low; for such a configuration: $4 < N_f < 120$ points. Consequently, the Echo spectra are not accurate and remain strongly altered by the time-windowing effect so that it is preferable to opt for a time analysis.

4.2. Roughness Parameter Inversion Method

The theoretical and numerical approaches show that the energy of the backscattered pressure depends on the surface statistics. Figures 4.9 illustrate the evolution of the RMS values of the Echo signal $\sqrt{\overline{E^2}}$ when scanning over the aluminum sample. This RMS value is calculated following Equation 4.3:

$$\sqrt{\overline{E^2}} = \sqrt{\frac{1}{N_t}\sum_{k=1}^{N_t} E^2(k)}\,. \qquad \textit{Eq 4.4}$$

Even if the scattered wave is not spherical, the RMS value of the pressure is assumed to be related to the wave energy. Numerical simulation shows that this ratio increases with the roughness. In addition the time waveform of the Echo signal is displayed for some typical RMS values. The time waveform inherits from the multiple random reflection and delays that occur in the scattering process (Figure 4.8). The size of the insonified area can be estimated knowing the length of the Echo and the incident angle; in that experiment $\partial D \approx 4 \cdot 10^{-4}$ m². Because the insonified area is longer than the scanning step, there is a 16% overlap on the scanning region.

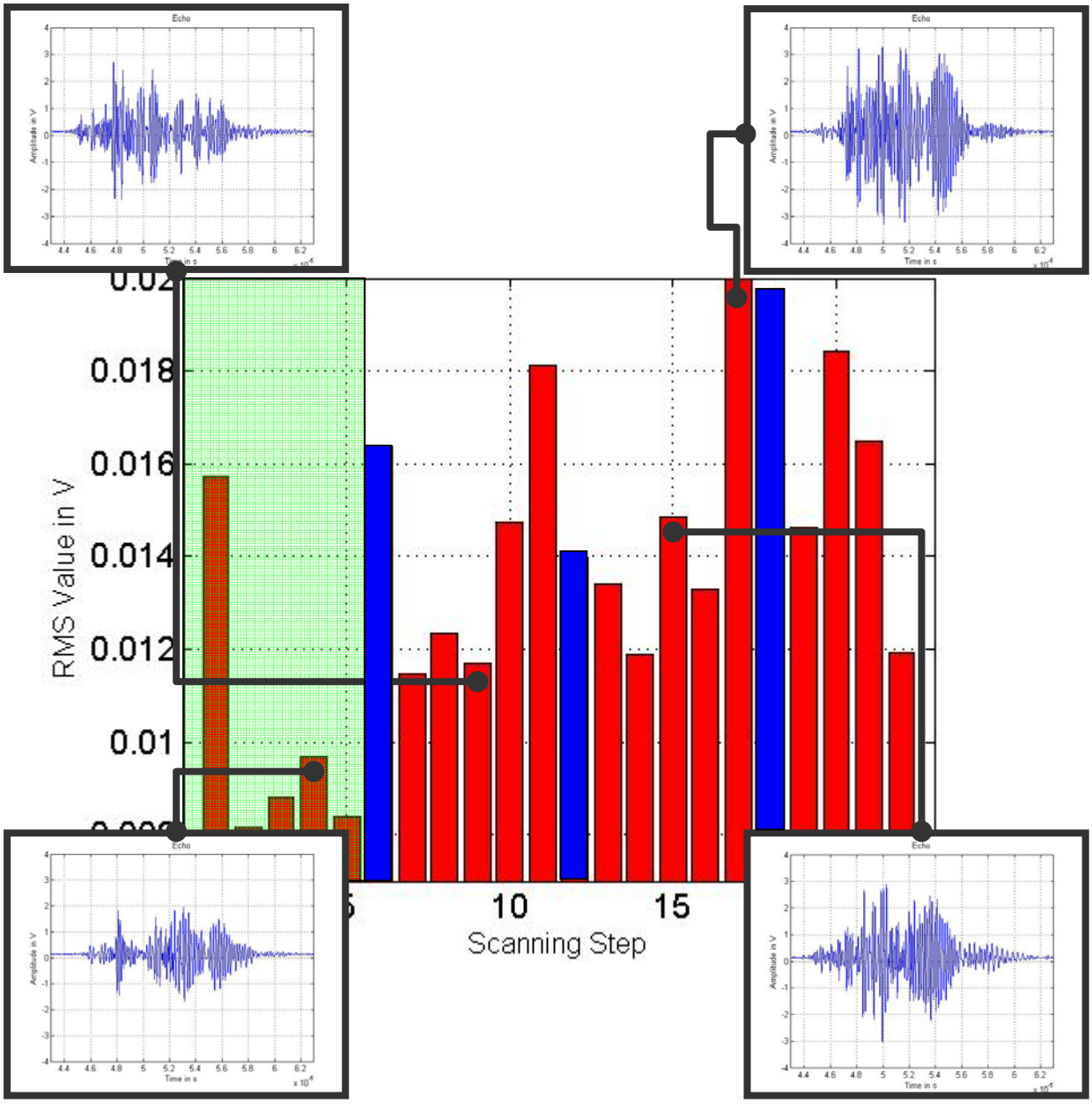

Figure 4.9 : Energy of the Backscattered Pressure

The spikes colored in blue correspond to the grooves that separate the different regions. A smooth surface generates low backscattering so that the shaded green area on Figure 4.9 corresponds to the non corroded region. The RMS value of the backscattered pressure appears to be a useful estimator when detecting corrosion. It is somehow related to the acoustic intensity magnitude.

The RMS measurements depend on the surface roughness parameters. Notwithstanding, many different waveforms can give the same RMS value and the detection system must be able to make the difference between every surface present in the tank.

It has been shown in Section 3 that the mean deviation of the scattered intensity can be estimated from the Helmholtz-Kirchhoff integral of the field [9]. While the ultrasonic transducer measures acoustic pressure and not intensity, this model is nevertheless a useful tool to infer surface roughness from the ultrasonic pulse. The time average intensity is described by a three-dimensional model whose polar and azimuth angles are respectively denoted by θ_2 and θ_3. The center of the insonified spot is located by $\vec{r}_c$. For a Gaussian roughness profile, the time average diffused intensity is given by Equation 3.22. A numerical study has been undertaken to characterize the effects of the three length scales on the scattered intensity. Introducing the following dimensionless ratios, $\alpha = \frac{\lambda_0}{\lambda}$ and $\beta = \frac{\sigma}{\lambda}$, one can rewrite Equation 3.22 as:

$$\langle I_d \rangle = \frac{4\pi^2\alpha^2 F^2 \exp\left(-4\pi^2\beta^2 C^2\right)}{4\pi\left|\vec{r}-\vec{r}_c\right|^2}\partial\overline{D}\sum_{n=1}^{\infty}\frac{\left(4\pi^2\beta^2 C^2\right)^n}{n!n}\exp\left(-\frac{4\pi^2\alpha^2\left(\mathrm{A}^2+\mathrm{B}^2\right)}{4n}\right).$$

Eq 4.5

For this study, the following values are used: $\left|\hat{\mathrm{R}}\right| = 1$, $\left|\vec{r}-\vec{r}_c\right| = 7.62\cdot10^{-2}$ m, and $\partial\overline{D} = 4\cdot10^{-4}$ m². The sum converges rapidly to a limit so that n =10 is sufficient.

4.2.1. Map of Scattered Intensity

The transducer has a finite diameter which acts as a spatial averaging filter. This is captured in the simulation by averaging the diffuse field over the transducer face. The normalized

amplitude of the backscattered intensity is calculated for values of α ranging from 0 to 3 and β ranging from 0 to 0.4. The results are shown on Figure 4.10. Clearly, maximum backscattering occurs in the region where α = 0.5 to 1.5 and β=0.1 to 0.25. Recalling that the typical frequency used in the experiment is 5 MHz, the corresponding order of magnitude for the roughness and the correlation length is respectively $6 \cdot 10^{-5} m$ and $3 \cdot 10^{-4} m$.

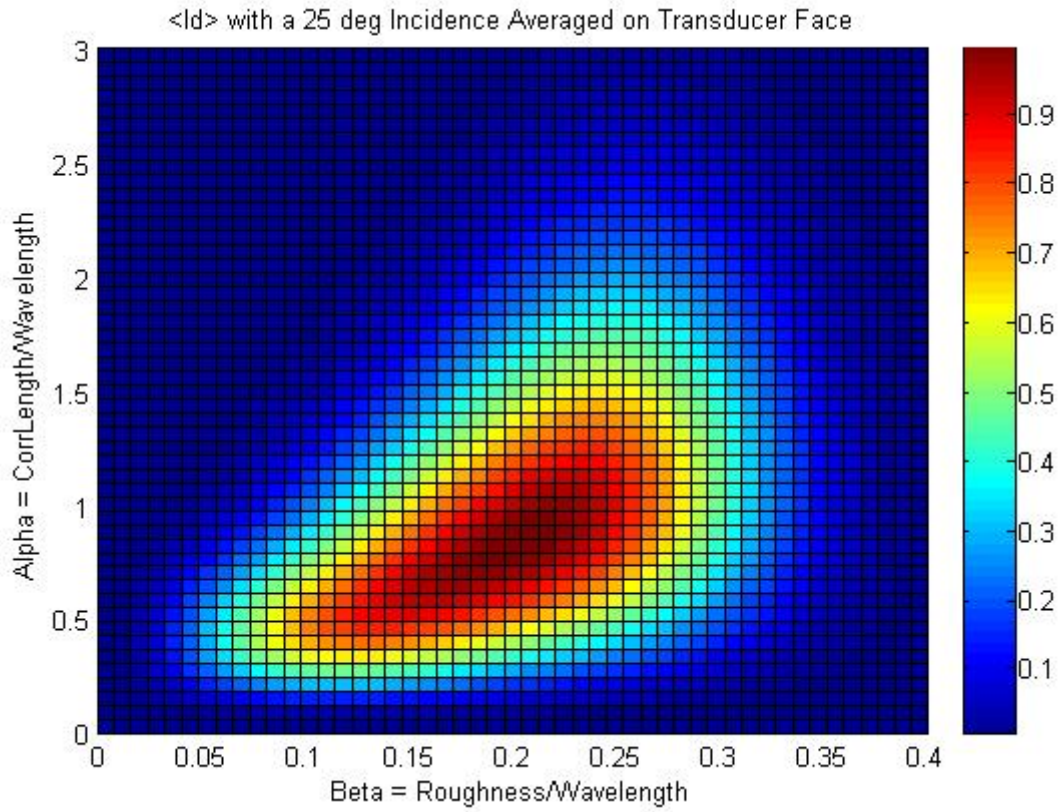

Figure 4.10 : Normalized Intensity as a Function of Alpha and Beta

The center of this region can be determined by numerically solving:

$$\frac{\partial}{\partial \alpha}\langle I_d \rangle = 0 \text{ and } \frac{\partial}{\partial \beta}\langle I_d \rangle = 0 . \qquad \textit{Eq 4.6}$$

Using an iteration method $(\alpha,\beta)=(0.7959,0.1959)$ is an approximate solution of the system above. This maximum value of the backscattered field can be observed on a directivity diagram (Figure 4.11).

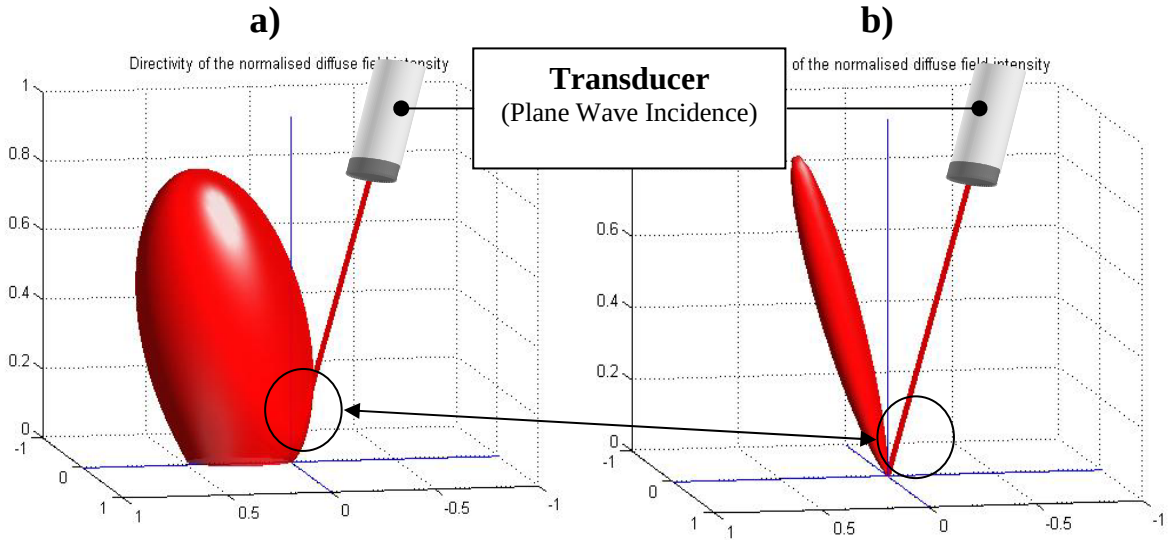

Figure 4.11 : Examples of High and Low Backscattering
a) Maximum Backscattering. **b)** Low Backscattering : $(\alpha,\beta)=(3,0.2)$.

Recalling that any type of surface is fully described by its coordinates (α,β), the basic approach is to use this map to find out what surface roughness verifies $\langle I_d(\alpha,\beta)\rangle = \langle I_d\rangle_{echo}$.

4.2.2. Uniqueness of the Solution

There are many solutions that satisfy $\langle I_d(\alpha,\beta)\rangle =$ constant . The solutions are contours where the intensity is constant. For example, assume that three types of surface noted A, B and C are present in the tank. According to Figure 4.12, Surfaces A and B are on the same intensity contour so that they could be mistaken for each other. By contrast, Surface C is clearly

distinctive. In this critical case, it is not possible to distinguish Surface A from Surface B: the solution is not unique. However, the map of intensity could be modified by changing the frequency or the angle of incidence so that the contour is displaced.

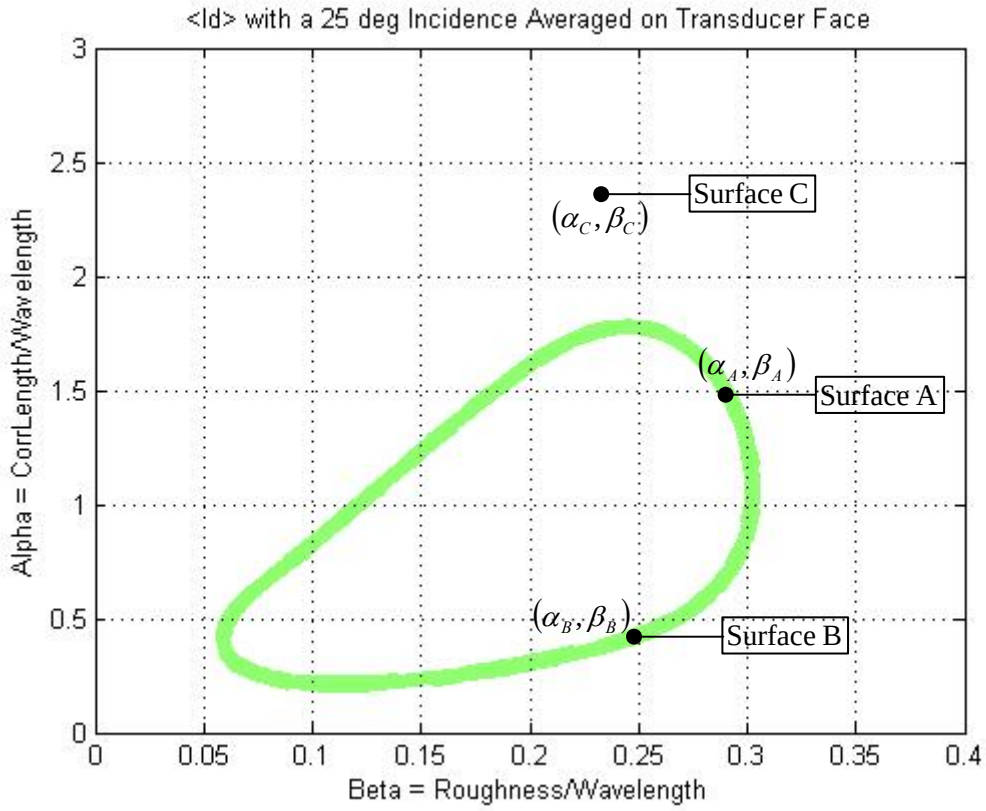

Figure 4.12 : Contour Plot at Id/Idmax = 0.4

On Figure 4.13, the angle of incidence has been set to 35° instead of 20°, resulting in a translation of the main pattern. All the solutions are now distinct: the experimental solution is unique. In a practical implementation, it will be preferable to calculate the map for various frequencies, using an FFT decomposition of the backscattered signal.

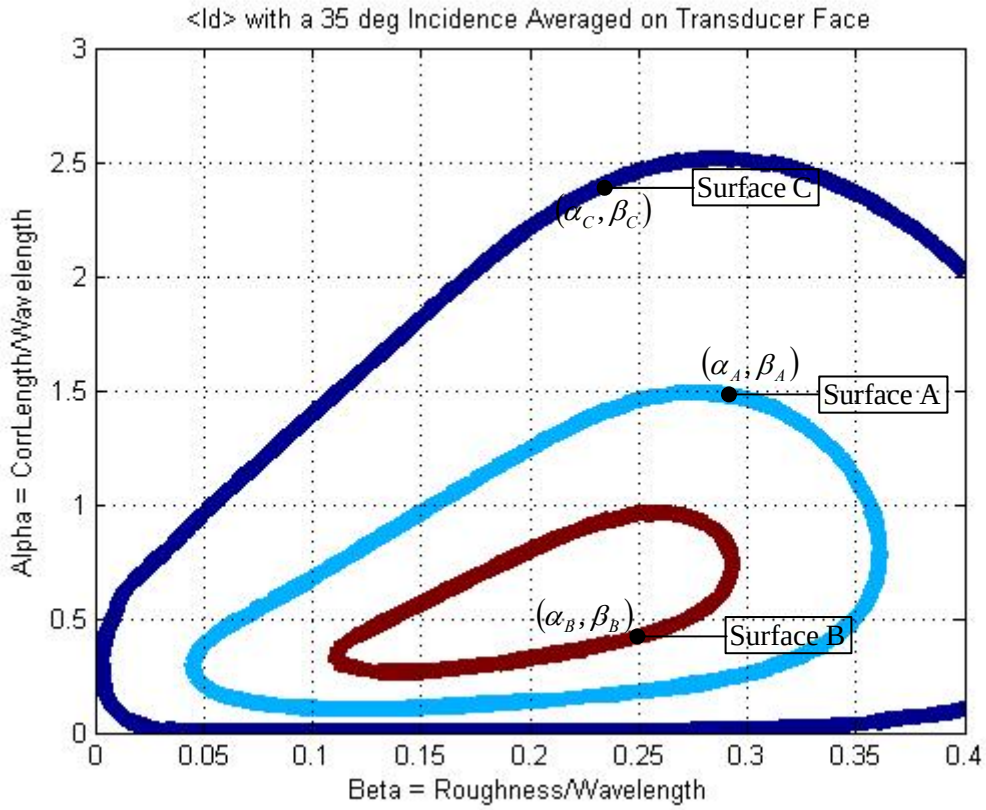

Figure 4.13 : Contour for a 35° Incidence

This map of intensity can be used if the transducer is far from the surface such that the scattered pressure is spherical. In that case, the RMS values shown on Figure 4.9, follows the behavior of the scattered intensity if the surface is Gaussian. If not, the relevance of those maps is not guaranteed.

4.3. Envelope Correlation Method

The envelope of the Echo waveform inherits from the scattering process that happens on the surface. Consequently, there exists a relation between the “shape” of the time signal and the type of scatterer. To emphasize this observation, the cumulated variance $\Xi(k)$ is computed for every Echo signals:

$$\Xi(k) = \frac{\sqrt{\sum_{n=1}^{k}\left(E(n) - \overline{E}\right)^2}}{\sqrt{\sum_{n=1}^{N_t}\left(E(n) - \overline{E}\right)^2}}, \qquad \textit{Eq 4.7}$$

where $\overline{E}$ is the average value of the Echo signal determined over N_t points:

$$\overline{E} = \frac{1}{N_t}\sum_{n=1}^{N_t} E(k). \qquad \textit{Eq 4.8}$$

$\Xi(k)$ tells about the evolution in time of the area under the Echo waveform. It is somehow related to its envelope. Figure 4.14 shows the evolution of the Echo signal E (blue curve) and its respective cumulated variance (red curve).

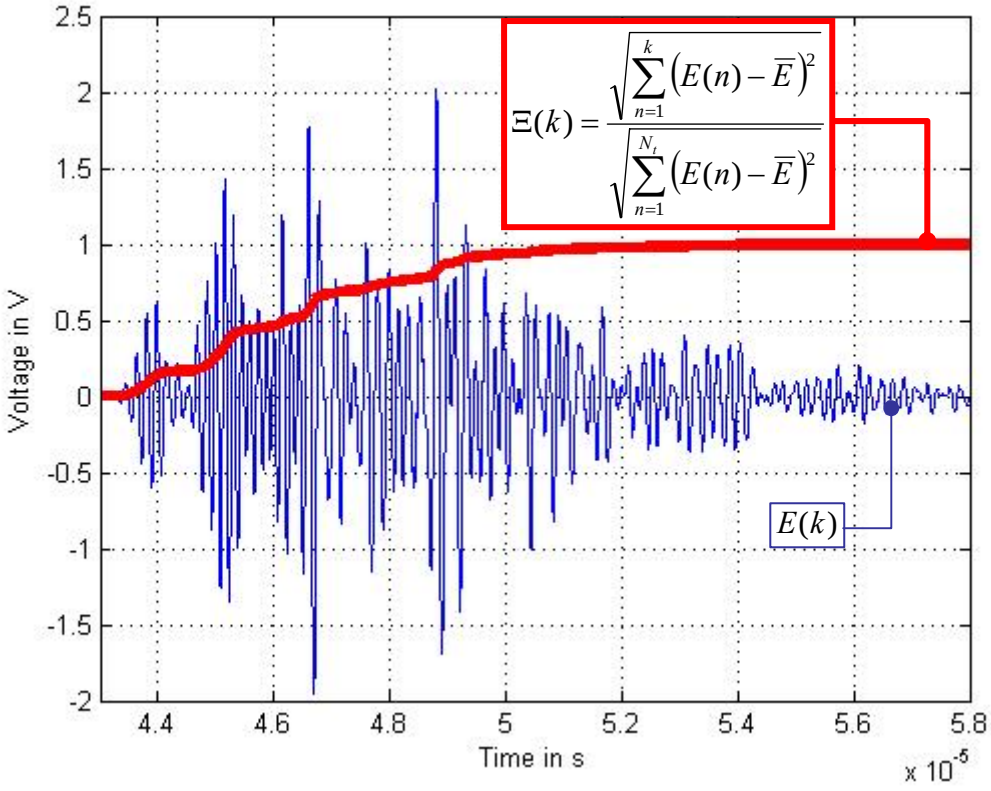

Figure 4.14 : Echo Waveform (Blue) and Its Cumulated Variance (Red)

Note that before computing the cumulated variance, the Echo signal is re-centered around zero by subtracting its mean value. The summation term on the numerator is not sensitive to the oscillations observed on the waveform. It is also normalized such that $\Xi(k)$ ranges from 0 to 1. $\Xi(k)$ is therefore related to the Envelope of the Echo waveform independently from its RMS value. The cumulated variance is fast to compute compared to the existing algorithms used to extract signal envelope.

It is relevant to compare the evolution of $\Xi(k)$ between the measurements done on the aluminum samples. Figure 4.15 illustrates the cumulated variance when scanning three types of scatterers, only the first 1000 points of the Echo are taken.

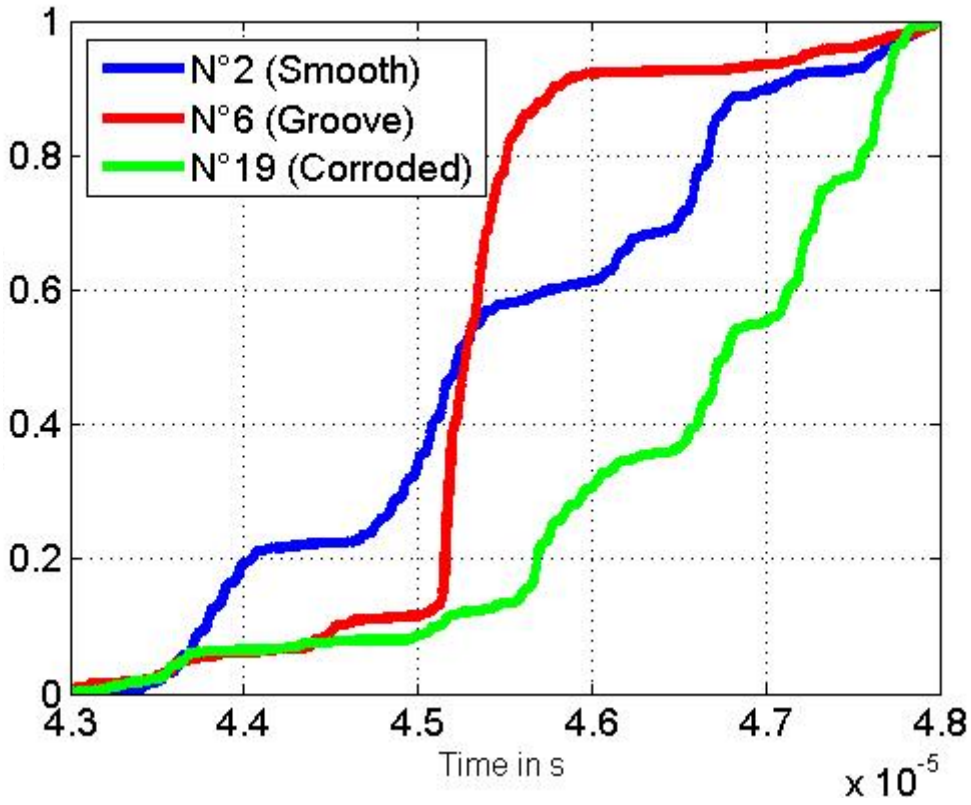

Figure 4.15 : Cumulated Variances When Scanning a Smooth Surface (Blue), a Surface with a Groove (Red) and a Corroded Surface (Green)

The evolutions shows on Figure 4.15 are typical for each type of scatterer. A fair way to compare how those curves differ is to compute the areas Λ between the cumulated variances. For two measurement *m* and *n*, this area is given as:

$$\Lambda_{m,n} = \sqrt{\frac{1}{N_t}\sum_{k=1}^{N_t}\left(\Xi_m(k) - \Xi_n(k)\right)^2} \; . \qquad \textit{Eq 4.9}$$

Equation 4.9 is analog to a covariance. Once all Λ's are computed, the 22 measurements are confronted each together in a 22 x 22 table on Figure 4.16 using Equation 4.9. This table shows how the Echo envelopes are correlated when scanning different type of surfaces.

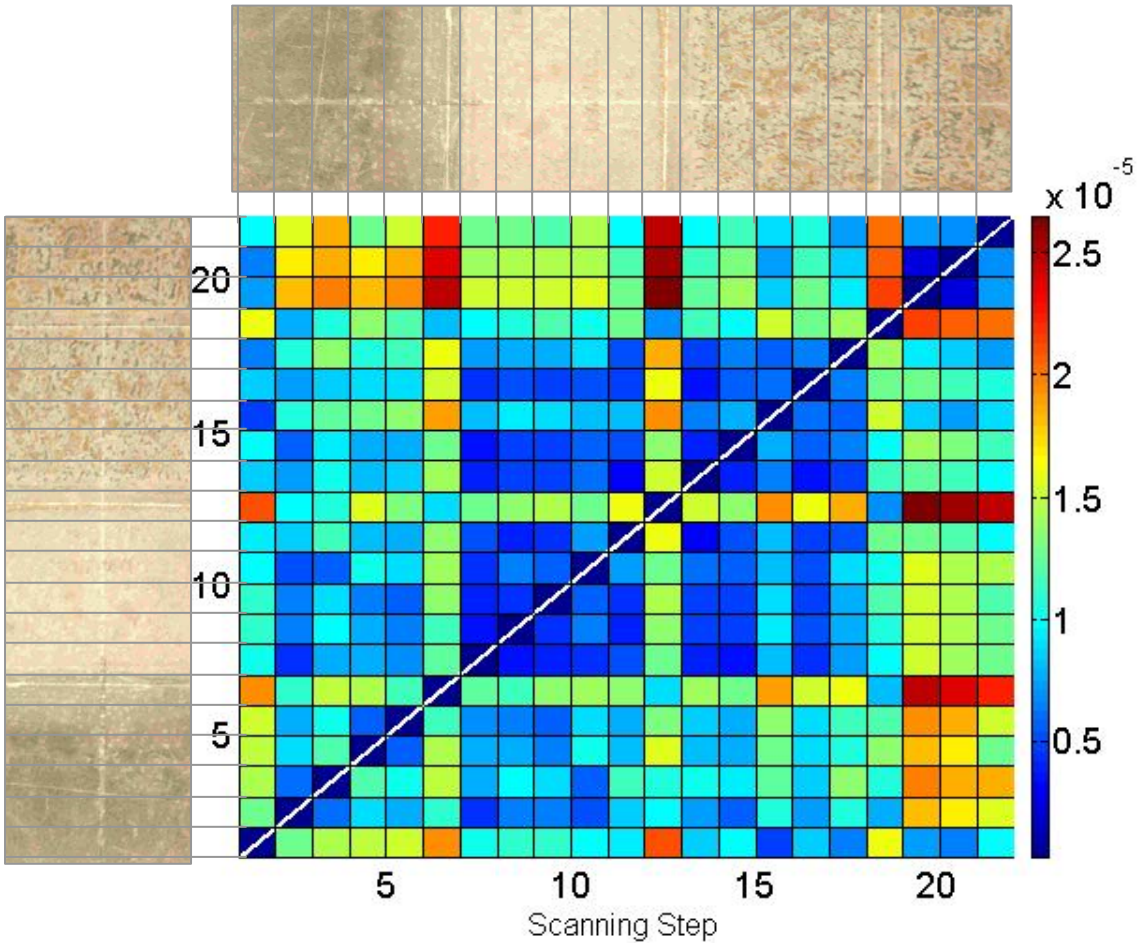

Figure 4.16 : Correlation between Envelopes of the Echo Waveform

The scanned regions are shown on the left side and at the top of the table. The higher the area Λ, the lower the correlation between Echo envelopes. The measurements 6, 12 and 18 involve the presence of a groove in the insonified spot, this shows up in the table by looking at the rows and columns 6, 12 and 18. It turns out that measurements involving local scatterers such as grooves and edges (Measurement 1) are more likely to be uncorrelated with the rest of the data. A method is dedicated to identify those scatterers in Section 4.4. Thus, Measurements 1, 6, 12 and 18 are removed from the table in order to observe the correlation between the data obtained from corroded and non corroded samples. The results are shown on Figure 4.17.

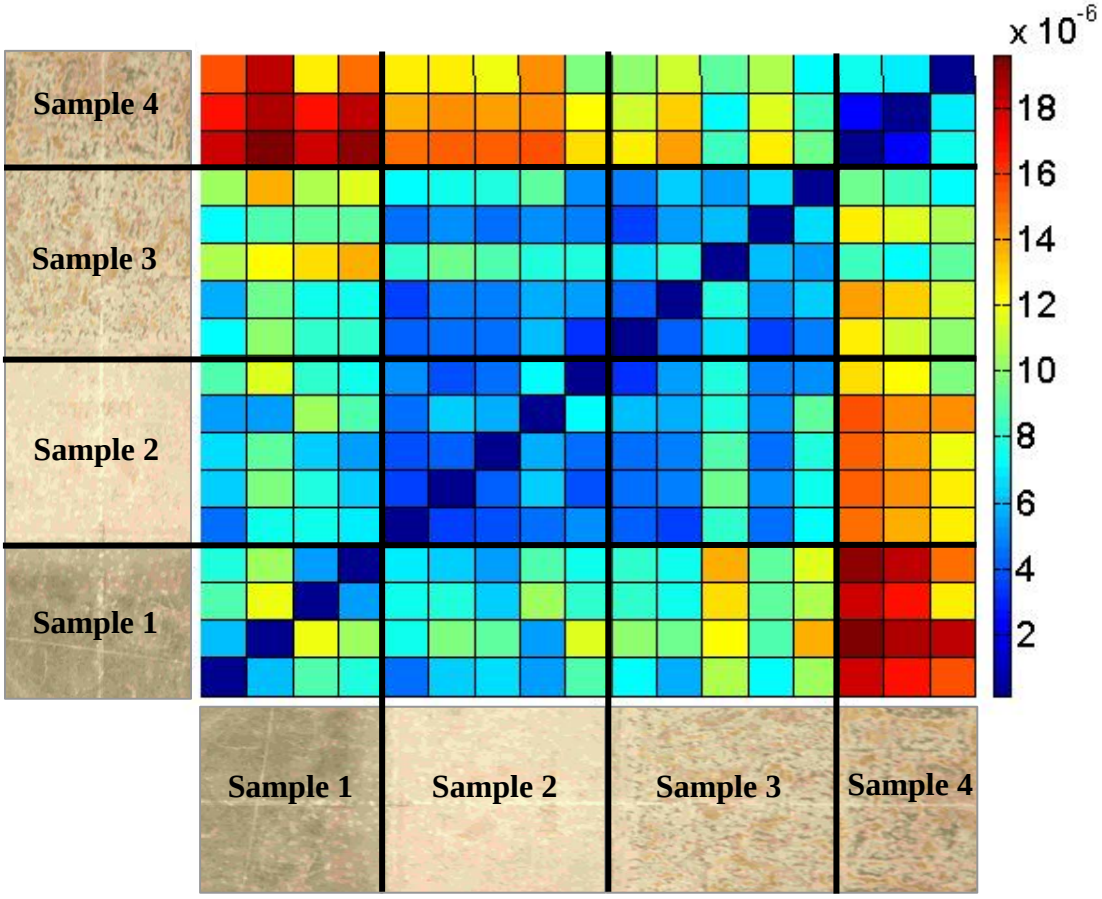

Figure 4.17 : Correlation between Envelopes of the Echo Waveform Once Local Scatterers Are Removed

The rows 15 to 17 (Sample 4) concern the most corroded part of the aluminum plate. One can see that the areas between cumulated variances are low when confronting the measurements done on Sample 4 as shown at the upper right corner of the table. Then Λ increases when moving toward Sample 1 (upper left corner of the table). In general, the value of Λ is low near the diagonal region when the samples are confronted to themselves. Figure 4.17 shows that the "shape" of the Echo differs between corroded and non corroded surfaces such that each scatterer has its typical Echo envelope. Equation is obtained from combining Equation and Equation . Because this method involves comparison between time waveforms, it has to be calibrated on the typical of surfaces encountered in the fuel tank.

As a second order estimator, the area between the cumulated variance of the Echo waveforms is a relevant in surface evaluation. Combined with the roughness inversion parameter method, the corrosion detection is emphasized by both energy of the backscattered field (first order) and Echo Envelope Correlation (second order). The next section introduces a complementary method used to identify local scatterers found in the fuel tank such as junctions edges or scratches.

4.4. Junctions and Partial Corrosion

The previous methods have been applied on samples that are quite uniform in their roughness properties. But the fuel tank shell is composed of several junctions, screws and corrosion stains that need a special treatment. Thus, the following approach proposes a method which can be used to identify those local scatters.

The Echo signal can be decomposed into several partitions with or without overlap. Each partition corresponds to the contribution in time of a given area of the insonified surface as shown on Figure 4.18. The spot and the Echo signal are cut into three parts, the blue arrows show which part of the spot are more likely to contribute in a given partition of the signal. Note that if the transducer is focused, the incidence varies upon the surface (orange arrows) such that each part of the spot depends on the local incidence and its distance from the transducer.

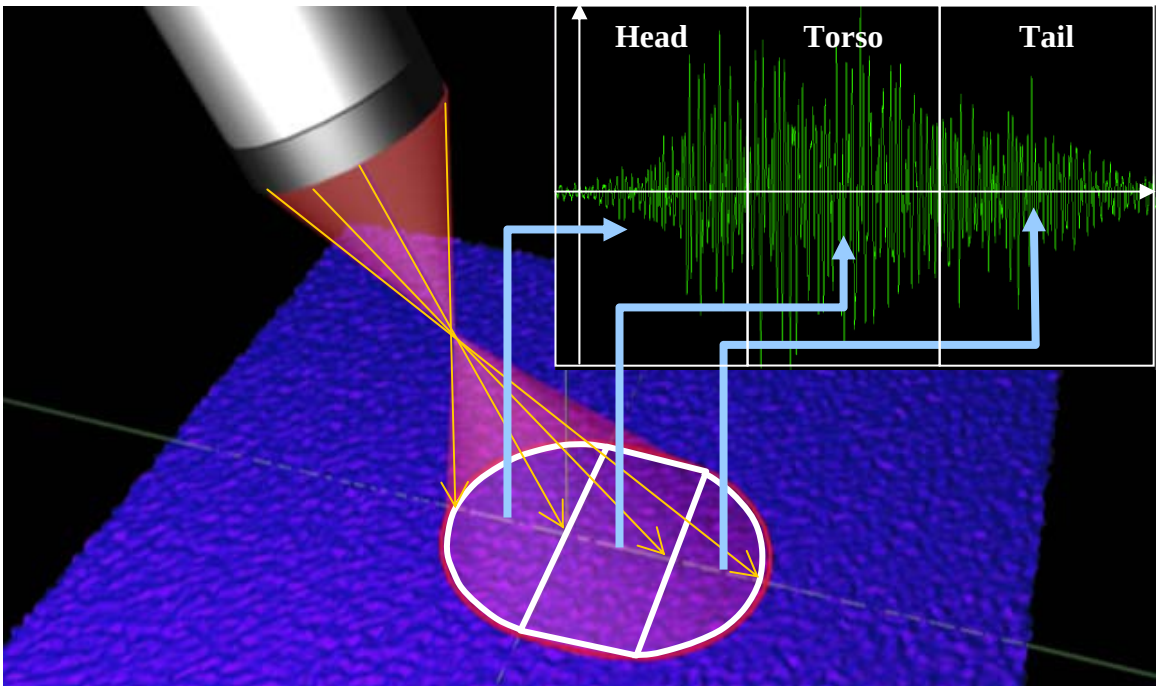

Figure 4.18 : Relation between Time and Space

When the entire insonified area contributes actively in the Echo signal (high roughness), the Echo waveform has a characteristic envelope which can be partitioned into three signals (Figure 4.18): the Head, the Torso and the Tail. The head signal is provided from a high incidence and a small time-to-flight between the surface and the transducer. At the opposite, the tail corresponds to a low incidence and a high distance from the transducer. Those three signals carry important information on the surface aspect and deserve an individual treatment. The Roughness Parameter Inversion Method and the Envelope Correlation Method can be applied respectively on each of those three signals.

Concerning the RMS value, measurement are placed in a 3-Dimensional space using the RMS values of the Head $\sqrt{\overline{E_1^2}}$, the Torso $\sqrt{\overline{E_2^2}}$ and the Tail $\sqrt{\overline{E_3^2}}$ as coordinates. Therefore, the distance between two measurements *m* and *n* is given by:

$$d_{mn} = \sqrt{\left(\sqrt{\overline{E_{1,m}^2}} - \sqrt{\overline{E_{1,n}^2}}\right)^2 + \left(\sqrt{\overline{E_{2,m}^2}} - \sqrt{\overline{E_{2,n}^2}}\right)^2 + \left(\sqrt{\overline{E_{3,m}^2}} - \sqrt{\overline{E_{3,n}^2}}\right)^2}. \qquad Eq\ 4.10$$

This distance tells how two measurements differ using the Echo RMS value. In order to illustrate the pertinence of this representation, the measurements are done by displacing a 10 MHz transducer whose focal length is 1 inch over six samples at 2 inches high from the surface with a 25° tilt angle (Figure 4.5). The surface samples are 3x3" squares of aircraft aluminum (Figure 4.19). As it has been done previously, different roughness scales are obtained from immersing the samples in solutions with different chlorine concentrations. The samples are numbered from 1 to 6 and described in Table 4.2.

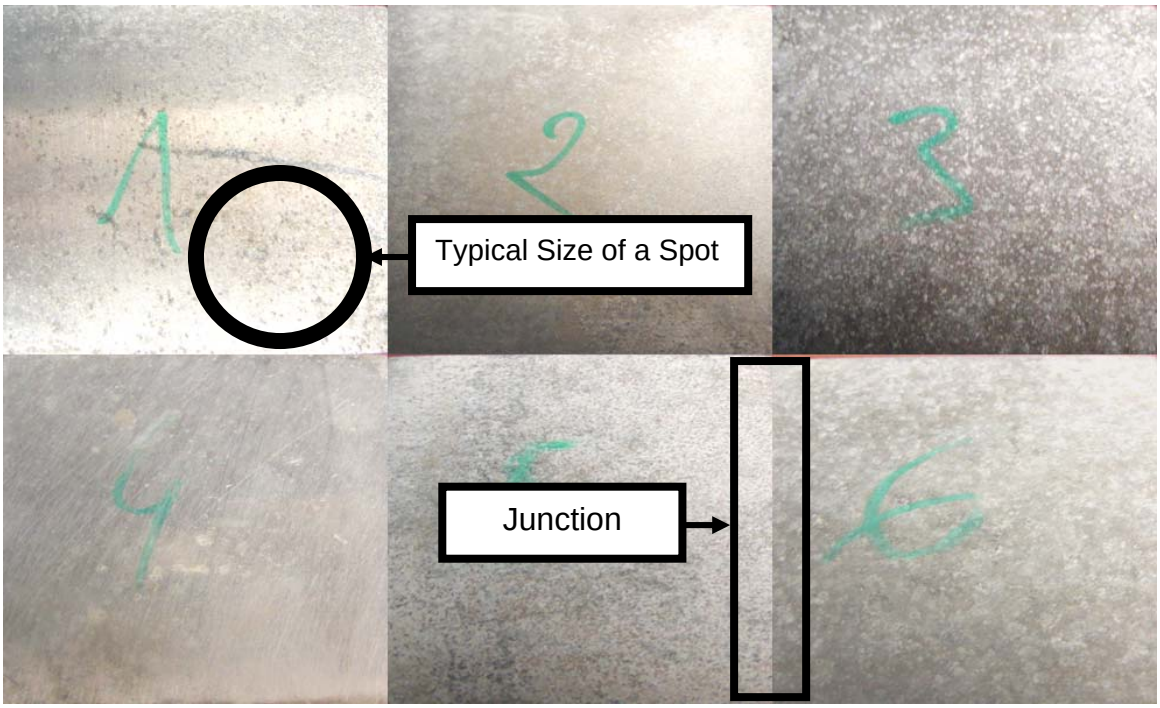

Figure 4.19 : Aircraft Aluminum Sample with Various Type of Corrosion Stages

Table 4.2 : Sample Description

Sample Number	Description
1	Smooth surface with soft pitting corrosion and corrosion initiated on machining marks.
2	Soft uniform corrosion
3	High uniform corrosion
4	Non corroded surface, reference.
5	Medium uniform corrosion
6	High uniform corrosion

3,000 measurements are done by traveling the scanner randomly over the sample. The Echo signal is divided into three parts equal in their length (1000 points). The realizations are placed in the RMS space on a real time plot. The presence of a junction or a scratch in the insonified area is manifested by a peak in the Echo waveform. As the transducer translate over the surface, the peak moves from the tail to the torso and then to the tail. Consequently, the RMS value of one of the three signals is abnormally increased by the presence of a peak. The presence of local scatterers such as junctions or local corrosion can be identified on Echo signals that have a noticeable disproportion in their envelope. Such a cause in the RMS space provokes a shift of the measurements toward one of the three axes as shown on Figure 4.20. The data provided by scanning junctions is easily removed by truncating the axis at some judicious values.

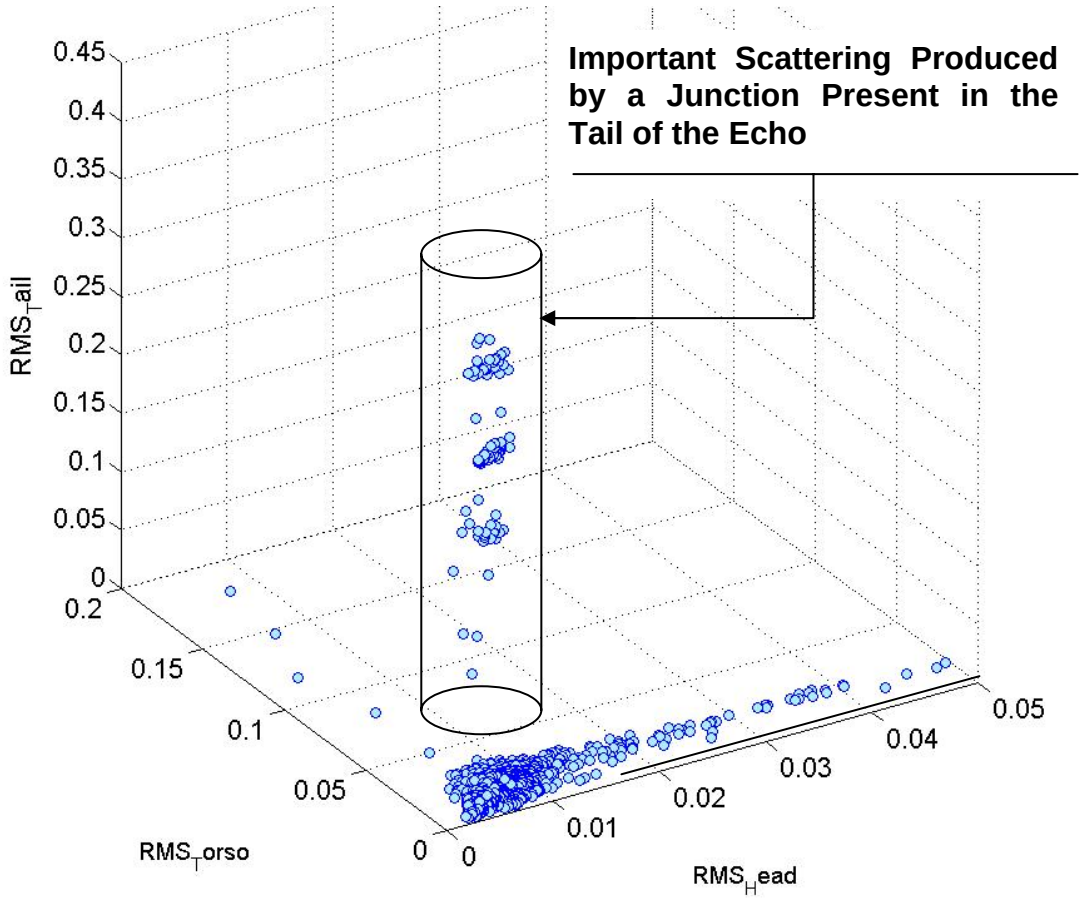

Figure 4. 20 : Representation of the Measurements in the RMS Space

In the RMS space, there exists a RMS range for each signal, head, torso and tail, that is typical of uniform corrosion. Experimentally, the mean proportion between those three signals is given in Table 4.3.

Table 4.3 : Echo Proportions

	Corroded Area	Non Corroded Area
Head	0.4297	0.5467
Torso	0.8264	0.6196
Tail	0.3640	0.5633

The values presented in this table are actually the components of the vector collinear to the regression lines displayed on Figure 4.21. The evolution is different depending if the surface is corroded or not, forming two distinct clouds. Therefore, two regression processes are carried out on the data. If the proportions presented in Table 4.3 are understood as shape factors, the red line describes the typical envelope of the Echo waveform for uniform corrosion. Deviation is allowed around the line for the sample to be assumed as uniformly corroded. Note that the samples that are partially corroded are more likely to be deviated from the mean line because only a part of the Echo waveform is privileged.

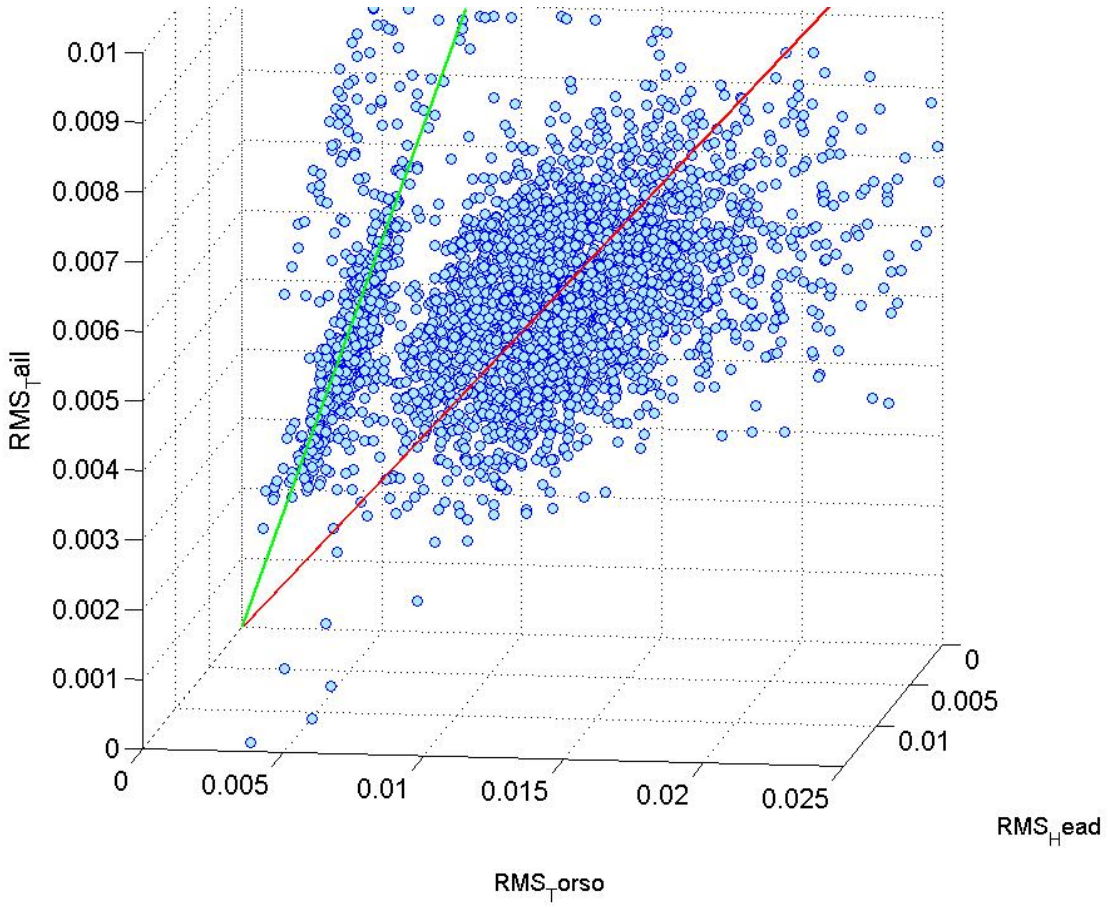

Figure 4.21 : Realizations without Important Local Scatterer

Thus, each type of scatterer spans distinct volumes in the RMS space; those volumes can be experimentally delimited in order to fix a criterion upon which it is possible to infer if:

- The surface is partially corroded or has a local scatterer such as the junctions encountered in the HB-53 fuel tank.
- The surface is or is not uniformly corroded

Those observations can be easily made when the insonified spot is important. A similar experiment has been done with a focal point close to the surface. The results are displayed on Figure 4.22. Because the measurements are extremely locally dependent in this configuration, it is more difficult to infer the presence of local scatterers.

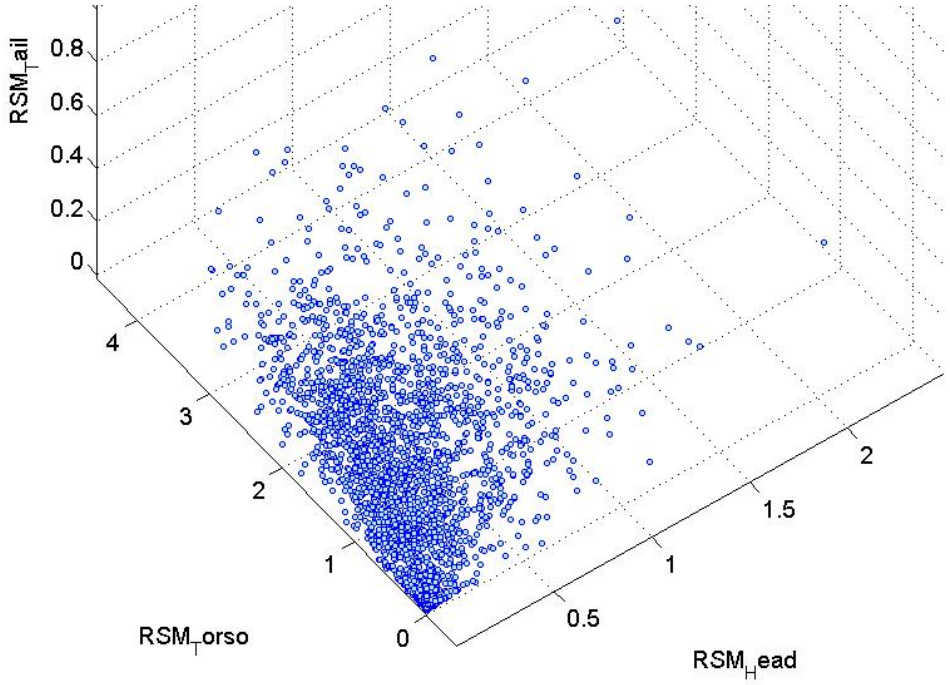

Figure 4.22 : RMS Representation of Measurements Done with a Small Insonified Area

Note that measurements can also represented into a correlation space using the Envelope Correlation Method. Using the distance between two measurements *m* and *n* it possible to know how a given measurement differ from the rest of the data:

$$d_{mn} = \sqrt{\Lambda_{1,mn}^2 + \Lambda_{2,mn}^2 + \Lambda_{3,mn}^2}\,, \qquad \textit{Eq 4.11}$$

where Λ_1, Λ_2 and Λ_3 are the areas computed following Equation 4.9 for the Head, the Torso and the Tail respectively.

Unfortunately, this representation can leads to contradictions in a 3 dimensional representation if one wants to visualize the overall data in the correlation space. In general, the RMS space is pertinent enough when evaluating the presence of local scatterers. The correlation space is potentially promising if the analysis has to be refined.

4.5. Finality of the Project: The Georgia Tech's NDE Scanning System

Some experiments realized in a GFE H53 fuel tank have shown that the more accurate transducer in terms of surface characterization is a 10 MHz, 0.5" diameter, focused transducer with 1.0 inch focal length. The frequency is adjusted with respect to the type of corrosion found in the tank. In addition, it is possible to obtain different resolution of scanning by displacing the focus above the surface. The size of the spot on the surface is changed and allows different types of scanning (Figure 4.23). The "overview" scan will be the baseline approach for inspection of extended corroded surfaces. The "detailed" approach is reserved for pits and scratches detection that will be the topic of some future experiments.

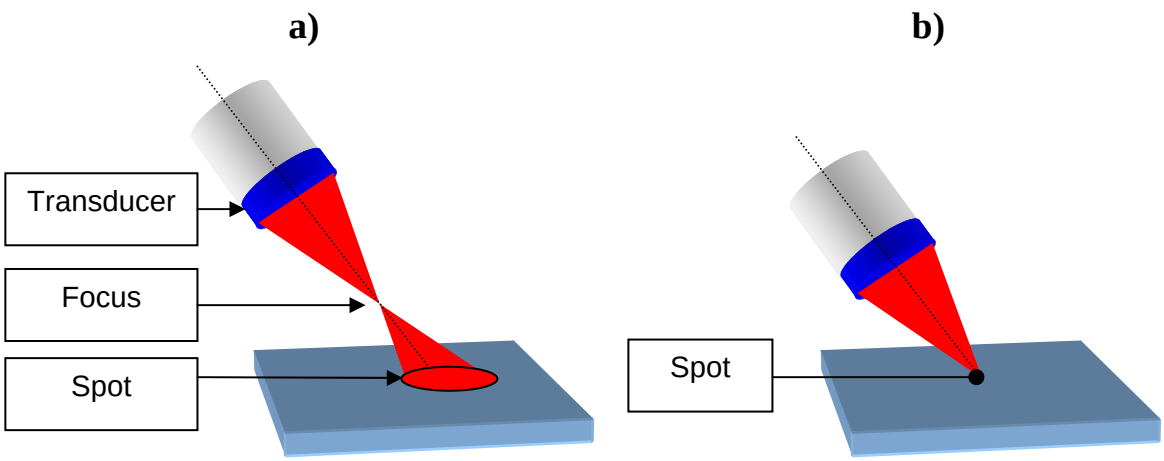

Figure 4.23 : Scanning Resolution Options
a) Overview Scan. **b)** Detailed Approach.

The method of ultrasound backscattering has been incorporated in the Georgia Tech's NDE scanning system developed at GTRI for this project. The system is a robot that can scan the bottom of the fuel tank via two degrees of freedom: one rotation and one translation along the longitudinal axis of the tank. The system is piloted using LabView software through a RS232 port. The Pulser/Receiver is still the Panametrics 5072 PR whereas the oscilloscope has been substituted by a NI5911[6] acquisition board which can be driven by LabView. Concerning the transducers, a V309-10 MHz whose focal length is 1 inch and a camera allows the system to superimpose acoustic data on the image of the scanned surface. Figure 4.24 shows the robot during the scanning process.

[6] A/D conversion : 100,000,000 samples / sec, 8 bits

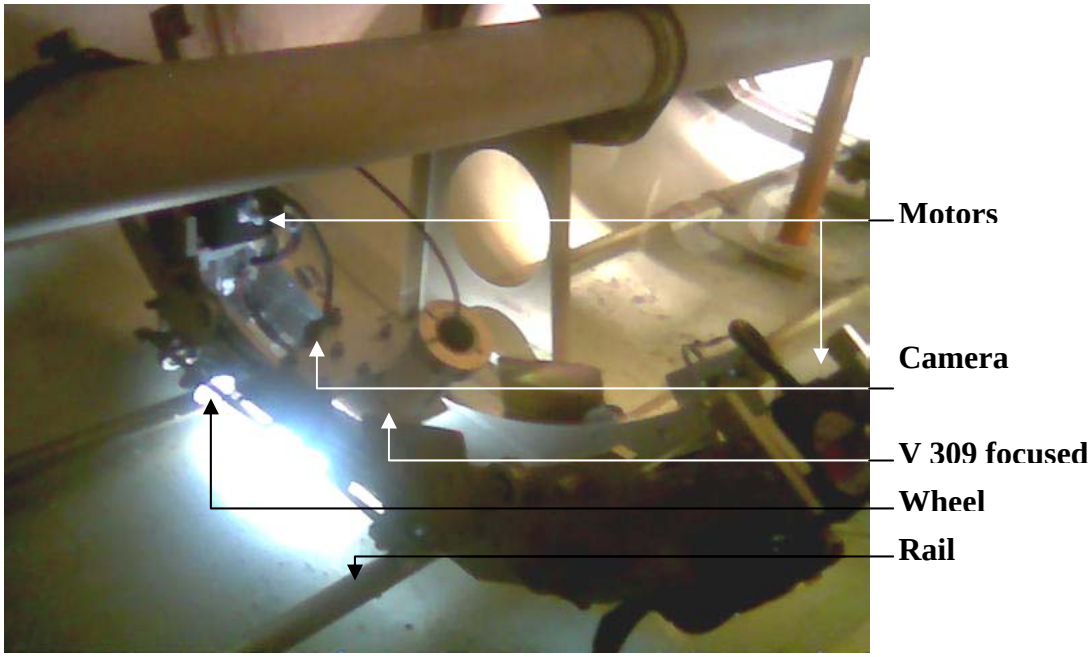

Figure 4.24 : Georgia Tech's NDE Scanning System, View from inside the Tank

A campaign of measurement has been achieved in real testing conditions at a military base[7] during a one week period by a team of GTRI personnel. It has not been possible to incorporate the envelope correlation and the inverse roughness parameter methods because they involve a calibration between numerical and preliminary experiments. The measurement mainly concerned RMS values of the backscattered pressure and it showed successful results in surface evaluation. NAVAIR is interested in further prototyping efforts for the following years to achieve fully operational detection of early corrosion in HB-53 fuel tanks.

[7] NAVY Depot, North Carolina

CONCLUSION

A system has been designed and tested to detect early corrosion the Aluminum liner inside a HB-53 fuel tank by measuring backscattered ultrasonic signals. From the first proof of concept in a fish tank to the field measurements in the HB-53 fuel tank at a NAVY depot, the elaboration of the Georgia Tech's scanning system took only a year to be completed. The design of the scanner prototype agrees with the methods presented in this document according to surface corrosion detection. The data issued from the backscattered wave is analyzed in the time domain using a first and a second order estimator. The Roughness Parameter Inversion Method relates the surface aspect and the RMS value of the backscattered signal involving the energetic aspect of the backscattered field. This method has already given satisfying results when combined to the video data. The RMS value of the backscattered pressure and the video data of the surface are superimposed such that the user can appreciate the depth of the surface relief. In addition, it has been possible to show the existence of a typical Echo envelope for corroded surfaces. The Envelope Correlation Method tracks a waveform signature of a corroded surface by comparing the signal envelope to a reference. Local scatterers such as edges and scratches found in the tank can be also identified by performing an envelope analysis. Thus, the inverse technique, the envelope correlation method and the detection of local scatterers are used to emphasized the presence of corrosion in the isonified area. Once combined in the system, those three methods and the

video data should give an efficient tool for corrosion detection in the H53 fuel tank for the future versions of the scanner.

REFERENCES

[1] Ogilvy, J. A. (1987). *Wave Scattering from Rough Surfaces*. Vol **50**, p.1553-1608. Report. On Progress in Physics.

[2] Kuperman, W.A., and Schmidt, H., (1989). *Self-Consistent Perturbation Approach to Rough Surface Scattering in Stratified Elastic Media.* Vol **86**, p.1511-1522. Journal of the Acoustical Society of America.

[3] Bass, F. G. and Fuks, I. M. (1979) *Wave Scattering from Random Statistically Rough Surfaces.* Pergamon, Oxford.

[4] Warren, P. D., Pecorari, C., Kolosov, O.V., Roberts, S. G. and Briggs, G. A. D. (1996). *Characterization of Surface Damage Via Surface Acoustic Waves.* Vol **7**, p.295-301. Nanotechnology.

[5] Bibber, J. W. *Corrosion Resistant Anodized Aluminum.* United States Patent 5,358,623 http://www.freepatentsonline.com/5358623.html.

[6] Roberge, R. P. Corrosion Doctors. http://www.corrosion-doctors.org. February 2006.

[7] Fontana, M. G. (1986) Corrosion Engineering. McGraw-Hill Book Co., NY.

[8] G. E. Simmers Jr. (2005), *Impedance-Based Structural Health Monitoring to Detect Corrosion*. Master's Thesis, Blacksburg, Virginia.

[9] Ogilvy, J. A. (1991). *Theory of Wave Scattering from Random Rough Surfaces.* Adam Hilger. Bristol, Philadelphia and New York.

[10] Dos Santos, S., Maréchal, P., Vander-Meulen, F. and Lethiecq, M. (2002). *Time-Frequency Analysis for Surface Roughness Characterization Using Backscatter Ultrasound.* Vol **21**, p.752-758. Review of Quantitative Nondestructive Evaluation.

[11] Chimenti, D. E., Nayfeh, A. H. and Butler, D., L. (1982*). Leaky Rayleigh Waves on a Layered Half-Space.* Vol **53**, p.170-176. Journal of Applied Physics.

[12] Glass, N.E. and Maradudin, A. A. (1983). *Leaky Surface-Elastic Waves on Both Flat and Strongly Corrugated Surfaces for Isotropic, Nondissipative Media.* Vol **54**, p.796-805. Journal of Applied Physics.

[13] Nayfeh, A. H., Chimenti, D. E., Laszlo, A. and Crane, R. L. (1981). *Ultrasonic LeakWaves in Presence of a Thin Layer.* Vol **52**, p.4985-4994. Journal of Applied Physics.

[14] Nayfeh, A. H., and Nagy P. B. (1997). *Excess Attenuation of Leaky Lamb Waves due to Viscous Fluid Loading.* Vol **101**, p.2649-2658. Journal of the Acoustical Society of America.

[15] Pecorari, C., Andrew, G. and Briggs, D. (1996). *Acoustic Microscopy and Dispersion of Leaky Rayleigh Waves on Randomly Rough Surfaces: A Theoretical Study.* Vol **43**, No 3, p.428-433. Transaction on Ultrasonics, Ferroelectrics and Frequency Control.

[16] Nagy, P. B. and Rose, J. H. (1993). *Surface Roughness and the Ultrasonic Detection of Subsurface Scatterers.* Vol **73**, p.566-580. Journal of Applied Physics.

[17] Zhu, W., Rose, J. L., Barshinger, J. N. and Agarwala, V. S. (1998*). Ultrasonic Guided Wave NDT for Hidden Corrosion Detection.* Vol **10**, p.205-225. Research in Nondestructive Evaluation.

[18] A. D. Pierce (1989). *Acoustics: An Introduction to Its Physical Principles and Applications.* Acoustical Society of America.

[19] Panametrics-NDT, *Technical Notes.* http://www.panametrics-ndt.com/ndt/ndt_transducers/downloads/transducer_technotes.pdf

[20] Kino, G. S. (1987). *Acoustic Waves: Devices, Imaging, and Analog Signal Processing.* Prentice Hall, INC. Englewood Cliffs, N. J.

[21] Ogilvy, J. A. (1988).*Computer Simulation of Acoustic Wave Scattering from Rough Surfaces.* Vol **21**, p.260-277. Journal of Physics D: Applied Physics.

[22] Silverman, B. W., (1986), *Density Estimation for Statistics and Data Analysis.* Chapman and Hall. London

[23] Vural,C., Sethares, W.A. *Blind Deconvolution of Noisy Blurred Images via Dispersion Minimisation.* http://eceserv0.ece.wisc.edu/~sethares/paperspdf/icassp02.pdf

[24] Breazeale, M. A., Laszlo, A. and Scott, G. W. (1977*). Interaction of Ultrasonic Waves Incident at the Rayleigh Angle onto a Liquid-Solid Interface.* Vol **48**, p.530-537. Journal of Applied Physics.

[25] Hansen, C. (2002). *Deconvolution and Regularization with Toeplitz Matrices.* Vol **29**, p.323-378. Numerical Algorithms. Kluwer Academic Publishers. Denmark.

[26] Simmers G. E. Jr., (2005). Impedance Based Structural Health Monitoring to Detect Corrosion. Thesis submitted to the Virginia Polytechnic Institute and State University.

[27] Wu, T. –T., Fang, J. –S. and Liu, P. –L. (1995*). Detection of the Depth of a Surface-Breaking Crack Using Transient Elastic Waves.* Vol **97**, p.1678-1686. Journal of the Acoustical Society of America.

[28] Zhao, Y.-P., Cheng, C-F., Wang, G.-C. and Lu, T.-M. (1998) *Characterization of Pitting Corrosion in Aluminum Films by Light Scattering.* Vol **73**, No 17, p.2431-2434. Applied Physics Letters. N.Y.

[29] Zhang, H. and Chimenti, D. E. (2000). *Two- and Three Dimensional Complex-Transducer-Point Analysis of Beam Reflection from Anisotropic Plates.* Vol **108**, p.2729-2737. Journal of the Acoustical Society of America.

[30] Montgomery, D. C. (2002). *Applied Statistics and Probability for Engineers* (3rd ed.). Arizona State University.

[31] Papoulis, A. (1991). *Probability, Random Variables, and Stochastic Processes* (3rd ed.). McGraw-Hill, INC. N.Y.

[32] Grinstead, C. M. and Snell, J. L. (1997). *Introduction to Probability. American Mathematical Society.* Providence, Rhode Island.

[33] Baeza-Yates, R., Glaz, J., Gzyl, H., Hüsler, J. and Palacios, J. L. (2005). *Recent Advances in Applied Probability.* Springer.

[34] Bruneau, M. (1998). *Manuel d'Acoustique Fondamentale.* Société d'Acoustique Française.